Electronic multicriticality in bilayer graphene

Vladimir Cvetkovic, Robert E. Throckmorton, and Oskar Vafek

National High Magnetic Field Laboratory and Department of Physics, Florida State University, Tallahasse, Florida 32306, USA

We map out the possible ordered states in bilayer graphene at the neutrality point by extending the previous renormalization group treatment of many-body instabilities to finite temperature, trigonal warping and externally applied perpendicular electric field. We were able to analytically determine all outcomes of the RG flow equations for the nine four-fermion coupling constants. While the full phase diagram exhibits a rich structure, we confirm that when forward scattering dominates, the only ordering tendency with divergent susceptibility at finite temperature is the nematic. At finite temperature, this result is stable with respect to small back and layer imbalance scattering; further increasing their strength leads to the layer antiferromagnet. We also determine conditions for other ordered states to appear and compare our results to the special cases of attractive and repulsive Hubbard models where exact results are available.

I. INTRODUCTION

Understanding itinerant electronic systems with competing ordering tendencies is among the most profound challenges in today's condensed matter theory. In one-dimensional systems, powerful theoretical tools are available for answering some of the questions,[1] but extending the techniques to higher dimensions has met with limited success. Often the problem is how to treat the various ordering tendencies on equal footing without an inherent bias toward any one of the possible ordered states.

In this regard, bilayer graphene at, and near, the neutrality point can be regarded as a model system. To a first approximation, there is a conduction band and a valence band that touch quadratically near two points, $\mathbf{K}$ and $\mathbf{K}' = -\mathbf{K}$, in the Brillouin zone.[2,3] Even when all electron-electron interactions are ignored, such a system would have low-temperature susceptibilities which diverge as $\sim \ln T$ toward a number of different ordered states. While there are no known exact solutions, such a situation is expected to lead to instabilities with respect to infinitesimal electron-electron interactions. The challenge is then to identify the conditions under which any one combination of the various possible states gets preferably selected as the temperature is lowered.

Since a many-body ordering appears already at weak coupling this problem is amenable to the renormalizaton group (RG) approach, whose advantage is that it can account for the competing tendencies in an unbiased way. Moreover, since the few-milli-electron-volt energy scales associated with ordering extracted from present-day experiments[4–10] are much smaller than the natural upper cutoff in the problem originating from the split-off bands derived from the dimerized sites ($\sim$200–300 meV), the physical system itself is expected to be well described by a weak coupling theory. Therefore we expect that the competition among the number of inherently strong-coupling phases can be accessed within such a weak coupling approximation.

The previous RG treatments of this problem presented in Refs. 11 and 12 consisted of first building a low-energy effective field theory, which when electron-electron interactions are neglected, can be thought of as a Gaussian fixed point of the RG scale transformation[13] with dynamical critical exponent $z = 2$.

Except under some nongeneric fine-tuned initial conditions, contact interactions have been shown to be marginally relevant at this fixed point. Such four-fermion terms in the low-energy effective field theory arise from microscopic electron-electron interactions $V_{ee}(\mathbf{r})$ whose Fourier transform is nondivergent in the small wave-vector limit. They could, for instance, correspond to $1/r$ Coulomb interactions screened by proximity to metallic gates. Within this approach, the electronic modes with momenta in a thin shell $(1 - \Delta\ell)\Lambda < |\mathbf{k}| < \Lambda$ near the cutoff Λ, and arbitrary frequency ω, are integrated out, while the change in the effective action is monitored as the process is iterated.[13,14] To determine the leading instability, infinitesimal symmetry breaking source terms were introduced[11,12,15] and included in the process of renormalization. The source term with the strongest divergence was then identified as the most dominant ordering tendency. In the case of purely forward scattering, or, in the notation of this paper, for $g_{A_{1g}}$ only, the leading instability was found to be toward the electronic nematic state. This state is gapless, with either two or four Dirac points near each $\mathbf{K}$ point depending on the strength of the order parameter. In the case of the Hubbard model, there is additional back scattering, $g_{E_{\mathbf{K}}} = \frac{1}{2}g_{A_{1g}}$, and layer imbalance scattering $g_{A_{2u}} = g_{A_{1g}}$, and the leading instability is found to be toward the layer antiferromagnetic state. The single-particle (electronic) spectrum of this phase is gapped.

In a similar approach,[16,17] the $1/r$ Coulomb interactions among the electrons in bilayer graphene were first screened using RPA, and then the full $\mathbf{q}$- and ω-dependent effective interaction was used as the initial condition for the subsequent Wilson-like RG treatment. While said approach can be criticized on the grounds that the screening of the long-range tail of the Coulomb interaction originates from integrating out electrons all the way down to the Fermi energy, which are double counted when reintroduced for the RG treatment, the results obtained using this approach are in qualitative agreement with the results obtained previously.[11,12]

To this end, we present an extension of the previous RG treatment of the problem to finite temperature[18–20] and finite externally applied perpendicular electric field. This allows us to include the competition between broken-symmetry phases with gaps in the electronic spectrum, which may be

energetically favorable, and gapless states, which may be entropically favorable. We also study the gradual suppression of an ordered state as the externally applied electric field is increased. Since temperature is treated explicitly, we can obtain the transition temperature directly, without making any of the *ad hoc* assumptions inherent in translating the value of the RG scale ℓ at which the couplings diverge into temperature.

As has been noted early on in the context of one-dimensional electron systems,[21,22] it is very useful to compare the results of an approximate RG approach to known exact results.[23–25] Despite the scarcity of exact results in higher dimensions, we can compare our results to some of the nontrivial properties of the Hubbard model at half-filling, which can be either established exactly[26–29] or can be obtained from Monte Carlo simulations.[30–32] In this regard, it was shown in Ref. [12] that starting with a repulsive Hubbard model on a honeycomb bilayer lattice at half-filling for $U \ll t_\perp \lesssim t$ leads to the layer antiferromagnet as the most dominant instability. In this work, we confirm the previous finding using the finite-temperature RG scheme. We further establish that, if we fix the value of the nine four-fermion coupling constants to correspond to the values derivable from the Hubbard model, then the low-energy effective field theory possesses the SO(4) symmetry of the microscopic Hubbard model.[28] As a consequence, for an attractive Hubbard model the result of our (approximate) RG analysis recovers the *exact* result that the s-wave superconducting order parameter can be continuously rotated to the "CDW" order parameter.[26,27] Since, for bilayer graphene, the charge-ordered state does not break the discrete translational symmetry of the lattice, it is not strictly a density wave, but rather corresponds to the layer-polarized state (LP). This can be seen in our RG equations; the LP and s_{++} superconducting source terms are identical provided that we start with the values of the four-fermion coupling constants corresponding to the Hubbard model with $U \ll t_\perp \lesssim t$. Moreover, since, in the weak coupling limit, we can map the microscopic lattice interactions to the four-fermion coupling constants in the continuum effective field theory, we can ask what happens when we add a b_1-b_2 interaction V in addition to the on-site attraction U (see Fig. [1]). When V is repulsive (attractive) we find that the exact degeneracy between the LP and s_{++} SC states is lifted in favor of the LP (s_{++} SC) as expected.[29,33]

Among the differences between our present approach and the related weak coupling approach employed in Refs. [16] and [17] is the fact that we perform our analysis at finite temperature, which leads to different RG equations for the couplings than at zero temperature. In addition to the advantages mentioned above, this allows us to systematically determine all possible outcomes of the RG equations in the nine-dimensional space of initial couplings. We also avoid screening the Coulomb interaction with the bilayer graphene low-energy degrees of freedom that enter our Wilson RG analysis. Rather, we assume that it is screened due to either finite temperature or the presence of external metallic gates. Finally, we do not rely on mean-field theory to determine the phases either directly from the bare couplings (i.e., without RG),[34–39] or on a renormalized mean-field treatment.[17] The shortcomings of other approaches[34,36] have been discussed in Ref. [17].
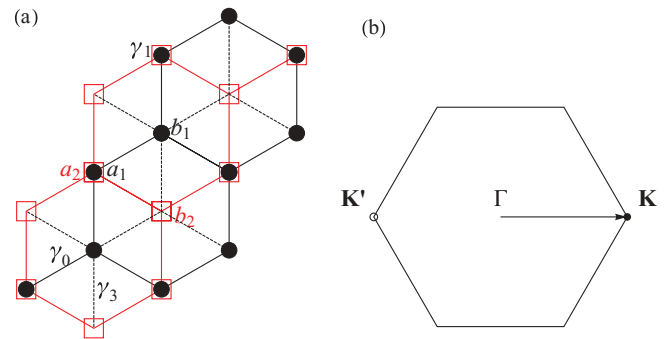

FIG. 1. (Color online) (a) The honeycomb bilayer lattice formed by bilayer graphene. We represent the bottom layer, 1, with black circles and the top layer, 2, with red squares. The a_i sites are the dimerized sites, and the b_i sites are the nondimerized sites. We include the nearest-neighbor intralayer hopping γ_0, the hopping between dimerized sites γ_1, and the nearest-neighbor interlayer hopping between nondimerized sites γ_3. (b) The Brillouin zone associated with the honeycomb bilayer with the parabolic degeneracy points $\mathbf{K} = \frac{4\pi}{3\sqrt{3}a}\hat{\mathbf{x}}$ and $\mathbf{K}' = -\mathbf{K}$ marked.

Within this formulation, as shown later in the text, the flow equations for the nine[12,16] coupling constants contain additional thermal factors, with an effective temperature T that grows under RG as $e^{2\ell}$. The flow equations (19) for the coupling constants describe two competing tendencies—the term proportional to a product of two four-fermion coupling constants tends to enhance their growth, while the thermal factors suppress the flow of the coupling. For any fixed initial couplings and at a high enough temperature, the couplings saturate to finite values as $\ell \to \infty$. As the temperature is lowered, the coupling constants saturate at higher, but still finite, values. At the transition temperature T_c, the coupling constants diverge as $\ell \to \infty$. Below T_c, the coupling constants diverge at a finite value of ℓ. The effects of trigonal warping, parametrized by a velocity v_3, can be readily included within this formalism as well.[16,17] Like temperature, trigonal warping tends to suppress the flow of the couplings. As a result, even at $T = 0$, a critical coupling strength must be exceeded for a phase transition to occur.[11,16] The strength of the critical coupling vanishes as v_3 vanishes.

The RG flow equations of the (infinitesimal) source terms for a multitude of symmetry-breaking order parameters reveal that, at the transition temperature, the source terms Δ acquire an anomalous dimension, η_Δ. Analysis of the free energy correction to $\mathcal{O}(\Delta^2)$ further reveals that, within this approximation, the physical susceptibility for a particular Δ diverges as $T \to T_c$ if $\eta_\Delta > 1$. Using this condition, we determine the phase diagram for different initial couplings (see Fig. [5]).

We find that, for purely forward electron-electron scattering, $g_{A_{1g}}$, the only order parameter with a divergent susceptibility at finite T is the nematic. Moreover, this is stable with respect to the presence of small, but finite, back scattering $g_{E_\mathbf{K}}$ and layer imbalance scattering (i.e., the difference between intra- and interlayer scattering) $g_{A_{2u}}$. Performing the analysis at finite temperature is crucial for revealing this stability. Upon increasing the back and layer imbalance scattering, the only other divergent susceptibility is toward a layer antiferromagnetic (AF) state. Reversing the sign of the backscattering while

fixing the layer imbalance scattering results in a quantum spin Hall state (QSH). Reversing the sign of the layer imbalance scattering while fixing the sign of the back scattering gives us a layer-polarized state (LP). Reversing the sign of both may lead to an s-wave superconductor. For small $g_{A_{2u}}/g_{E_\mathbf{K}}$ and $g_{E_\mathbf{K}} \approx g_{A_{1g}} > 0$, we may find a Kekulé current state (KC). These results are summarized in Fig. 5, which shows the phase diagram in the space of initial $g_{A_{1g}}$, $g_{E_\mathbf{K}}$, and $g_{A_{2u}}$.

Remarkably, the flow equations for the nine coupling constants can be analyzed in their entirety at T_c. We find that, if a coupling constant diverges, it grows as $e^{2\ell}$. At the same time, the ratios of the coupling constants may either approach values determined by a two-parameter family of functions, which we call the target plane, or four isolated fixed ratios that do not belong to the fixed plane. For each of these cases, we determine the symmetry-breaking channels with divergent susceptibilities at T_c. The results are summarized in Fig. 9.

The rest of the paper is organized as follows. In Sec. II, we present our model for the system. Section III is dedicated to the thorough analysis of the RG equations and our main results. Section IV deals with the effects of an applied perpendicular electric field on the phase boundaries. Our conclusions are presented in Sec. V. We give details of our derivations in the Appendices.

II. HAMILTONIAN

We will be employing a low-energy effective theory for the bilayer graphene lattice. This lattice and the associated Brillouin zone are shown in Fig. 1. Our model includes the nearest-neighbor intralayer hopping $\gamma_0 \equiv t$, the hopping between dimerized sites $\gamma_1 \equiv t_\perp$, and the nearest-neighbor interlayer hopping between nondimerized sites γ_3. It is this last hopping that is responsible for trigonal warping. Experimentally,[40] $\gamma_0 \approx 3$ eV, $\gamma_1 \approx 0.4$ eV, and $\gamma_3 \approx 0.3$ eV. Throughout this paper, we will use units in which $k_B = \hbar = 1$.

A. Noninteracting Hamiltonian

The tight-binding model for the lattice described above is[3]

$$H_{\text{tb}} = -\gamma_0 \sum_{\mathbf{R},\delta,\sigma} [a_{1\sigma}^\dagger(\mathbf{R})b_{1\sigma}(\mathbf{R}+\delta) + a_{2\sigma}^\dagger(\mathbf{R})b_{2\sigma}(\mathbf{R}-\delta)$$
$$+ \text{H.c.}] - \gamma_1 \sum_{\mathbf{R},\sigma} [a_{1\sigma}^\dagger(\mathbf{R})a_{2\sigma}(\mathbf{R}) + \text{H.c.}]$$
$$- \gamma_3 \sum_{\mathbf{R},\delta',\sigma} [b_{1\sigma}^\dagger(\mathbf{R}+\delta)b_{2\sigma}(\mathbf{R}+\delta+\delta') + \text{H.c.}], \quad (1)$$

where $(a,b)_{m\sigma}(\mathbf{r})$ annihilates an electron on the (a,b) sublattice on layer m and site $\mathbf{r}$ with spin σ. The vectors $\mathbf{R}$ are the positions of the dimerized sites within a unit cell, and δ represents one of three vectors connecting an a_1 site with a nearest-neighbor b_1 site. The possible values of δ are $-\frac{\sqrt{3}}{2}a\hat{\mathbf{x}} + \frac{1}{2}a\hat{\mathbf{y}}$, $\frac{\sqrt{3}}{2}a\hat{\mathbf{x}} + \frac{1}{2}a\hat{\mathbf{y}}$, and $-a\hat{\mathbf{y}}$, where the lattice constant $a \approx 1.4$ Å. Whenever there is a sum on δ, we sum over these three values; if δ appears without a summation over it, on the other hand, then we choose one of these three values for it.

We may derive our low-energy effective theory for the above system by either projecting out the high-energy modes[41]

or equivalently by writing the above theory as a coherent-state path integral, integrating out the dimerized sites,[12,15] and expanding around the $\mathbf{K}$ and $\mathbf{K}'$ points. The resulting theory is

$$\mathcal{H} = \mathcal{H}_0 + \mathcal{H}_{\text{int}}, \quad (2)$$

where

$$\mathcal{H}_0 = \sum_{|\mathbf{k}|<\Lambda} \sum_{\sigma=\uparrow,\downarrow} \psi_{\mathbf{k}\sigma}^\dagger H_\mathbf{k} \psi_{\mathbf{k}\sigma}. \quad (3)$$

In the above Hamiltonian, the Fermi spinor, which describes the modes in the vicinity of the $\pm\mathbf{K}$ points and concentrated at b sites in layers 1 and 2, is

$$\psi_{\mathbf{k}\sigma} = \begin{pmatrix} \psi_{\mathbf{K}\sigma}^{(b_1)}(\mathbf{k}) \\ \psi_{\mathbf{K}\sigma}^{(b_2)}(\mathbf{k}) \\ \psi_{-\mathbf{K}\sigma}^{(b_1)}(\mathbf{k}) \\ \psi_{-\mathbf{K}\sigma}^{(b_2)}(\mathbf{k}) \end{pmatrix}. \quad (4)$$

The first of the two matrices in Eq. (3) describes the parabolic dispersion and the second is a linear term that results in trigonal warping:

$$H_\mathbf{k} = H_\mathbf{k}^{(2)} + H_\mathbf{k}^{(tw)}, \quad (5)$$

$$H_\mathbf{k}^{(2)} = \frac{1}{2m^*}\left[(k_x^2 - k_y^2)\Sigma_x + 2k_x k_y \Sigma_y\right], \quad (6)$$

$$H_\mathbf{k}^{(tw)} = v_3\left(k_x\Lambda_x + k_y\Lambda_y\right), \quad (7)$$

where

$$\Sigma_x = 1\sigma_1, \quad \Sigma_y = \tau_3\sigma_2, \quad (8)$$

$$\Lambda_x = \tau_3\sigma_1, \quad \Lambda_y = -1\sigma_2. \quad (9)$$

In terms of the tight-binding parameters in our lattice Hamiltonian, the effective mass m^* is

$$m^* = \frac{2\gamma_1}{9a^2\gamma_0^2} \quad (10)$$

and the trigonal warping velocity v_3 is

$$v_3 = 3a\gamma_3. \quad (11)$$

Experimentally,[6,7] $m^* \approx 0.029 m_e$, while the value that we obtain from the above formula and the experimental values of the hopping parameters given above is $m^* \approx 0.038 m_e$. The value of the trigonal warping velocity used in fitting the experimental data[6] is $v_3 \approx 1.41 \times 10^5$ m/s, while that obtained from the above formula is $v_3 \approx 1.91 \times 10^5$ m/s (Ref. 16 assumes a value of $v_3 = 10^5$ m/s). The origin of these admittedly unimportant and small discrepancies is unclear at this time.

B. Symmetry classification

The space group symmetry operations, which leave the Hamiltonian invariant at the Γ point form a point group D_{3d}. Similarly, at the $\pm\mathbf{K}$ points, the symmetry operations form a

point group D_3. The character tables[42] of these two groups are shown below.

$\mathbf{D_{3d}}$	E	$2C_3$	$3C_2'$	i	$2S_6$	$3\sigma_d$
A_{1_g}	1	1	1	1	1	1
A_{2_g}	1	1	-1	1	1	-1
E_g	2	-1	0	2	-1	0
A_{1_u}	1	1	1	-1	-1	-1
A_{2_u}	1	1	-1	-1	-1	1
E_u	2	-1	0	-2	1	0

$\mathbf{D_3}$	E	$2C_3$	$3C_2'$
A_1	1	1	1
A_2	1	1	-1
E	2	-1	0

The sixteen 4×4 matrices that operate in the layer and $\pm\mathbf{K}$ valley space, can be grouped based on their transformation properties under these group operations. We find that

$$A_{1g}+ : 1_4,$$
$$A_{2g}- : \tau_3\sigma_3,$$
$$E_g+ : (1\sigma_1, \tau_3\sigma_2),$$
$$A_{1u}- : \tau_3 1,$$
$$A_{2u}+ : 1\sigma_3,$$
$$E_u- : (\tau_3\sigma_1, -1\sigma_2),$$
$$A_{1\mathbf{K}}+ : \tau_1\sigma_1; \tau_2\sigma_1,$$
$$A_{2\mathbf{K}}- : \tau_1\sigma_2; \tau_2\sigma_2,$$
$$E_{\mathbf{K}}+ : (\tau_1 1, -\tau_2\sigma_3; -\tau_2 1, -\tau_1\sigma_3).$$

The $\pm$ next to the name of the representation denotes whether the particular operator is even or odd under time reversal symmetry. An equivalent classification can be found in Ref. 17, though the notation is different.

C. Interaction Hamiltonian

As shown previously, assuming the microscopic lattice interactions are falling off faster than $1/r^2$, there are nine marginal interaction couplings at the Gaussian fixed point when $T = 0$ and $v_3 = 0$. The interaction term in the Hamiltonian is therefore

$$\mathcal{H}_{\text{int}} = \frac{1}{L^2} \sum_S \frac{g_S}{2} \sum_{\mathbf{k},\mathbf{k}',\mathbf{q}} \sum_{\sigma,\sigma'} \psi_{\mathbf{k}\sigma}^\dagger S \psi_{\mathbf{k}+\mathbf{q},\sigma} \psi_{\mathbf{k}'\sigma'}^\dagger S \psi_{\mathbf{k}'-\mathbf{q},\sigma'}. \tag{12}$$

The sum over S includes the 16 matrices belonging to the nine representations. Since the couplings for the squares of the operators belonging to the same representation must be the same, we have nine independent couplings. So, for example, for the E_g representation, the corresponding interaction term is schematically $\frac{1}{2}g_{E_g}[(\psi_\sigma^\dagger 1\sigma_1\psi_\sigma)^2 + (\psi_\sigma^\dagger \tau_3\sigma_2\psi_\sigma)^2]$.

We may think of $g_{E_{\mathbf{K}}}$ as representing backscattering, $g_{A_{1g}} + g_{A_{2u}}$ as representing intralayer scattering, and $g_{A_{1g}} - g_{A_{2u}}$ as representing interlayer scattering, as is demonstrated in our previous work.[15] If we introduce a density-density interaction $V(\mathbf{r})$ into the microscopic tight-binding Hamiltonian, then

the forms of these couplings are given by Eqs. (119)–(121) in Ref. 15, where they are denoted by g_{A_1}, g_{C_1}, and g_β, respectively.

As we will see shortly, if we start with these three couplings, then the other six will be generated under RG. All nine couplings may also be thought of as interactions between local fluctuations of different order parameters.

III. FINITE-TEMPERATURE RENORMALIZATION GROUP

We are interested in introducing the temperature T and the trigonal warping velocity v_3 explicitly into our renormalization group transformations. To proceed, we rewrite the partition function as a coherent-state Grassman path integral:

$$Z = \int \mathcal{D}(\psi^*, \psi) e^{-S_0 - S_{\text{int}}}, \tag{13}$$

where

$$S_0 = \frac{1}{\beta} \sum_{n=-\infty}^{\infty} \sum_{|\mathbf{k}|<\Lambda} \sum_{\sigma=\uparrow,\downarrow} \psi_{\mathbf{k}\sigma}^\dagger(\omega_n)(-i\omega_n + H_{\mathbf{k}})\psi_{\mathbf{k}\sigma}(\omega_n),$$

n is an integer, and the Matsubara frequency is $\omega_n = (2n+1)\pi T$. The interaction term is

$$S_{\text{int}} = \frac{1}{2} \int_0^\beta d\tau \int d^2\mathbf{r} \sum_S g_S \left[\sum_\sigma \psi_\sigma^\dagger(\mathbf{r},\tau) S \psi_\sigma(\mathbf{r},\tau) \right]^2 \tag{14}$$

and

$$\psi_\sigma(\mathbf{r},\tau) = \frac{1}{\beta} \sum_{n=-\infty}^{\infty} \frac{1}{L} \sum_{|\mathbf{k}|<\Lambda} e^{-i\omega_n\tau} e^{i\mathbf{k}\cdot\mathbf{r}} \psi_{\mathbf{k}\sigma}(\omega_n). \tag{15}$$

Equivalently, we may write the interaction term as

$$S_{\text{int}} = \frac{1}{2} \int_0^\beta d\tau \int d^2\mathbf{r} \sum_{j=1}^9 g_j \sum_{m=1}^{m_j} \left[\psi^\dagger(\mathbf{r},\tau) \Gamma_j^{(m)} \psi(\mathbf{r},\tau) \right]^2. \tag{16}$$

Note the absence of explicit spin subscripts on the (eight-component) $\psi = (\psi_\uparrow, \psi_\downarrow)^T$ fields. The $\Gamma_j^{(m)}$ matrices are defined in Eqs. (C7)–(C15), and m_j is the multiplicity of the jth representation.

Our renormalization group procedure consists of splitting the ψ fields into fast and slow modes and progressively integrating out the fast modes with momenta restricted to the small shell $\Lambda(1 - \Delta\ell) < |\mathbf{k}| < \Lambda$ with no restriction on the Matsubara frequencies ω_n. After each such mode elimination, we choose to rescale the momenta in the effective action for the slow modes such that the new cutoff is again Λ and that the $H_{\mathbf{k}}^{(2)}$ term is left invariant. If we also wish to keep the $i\omega_n$ term invariant, and take $\Delta\ell$ to be infinitesimal, we find that the temperature and the trigonal warping velocity flow under RG as

$$\frac{dT}{d\ell} = 2T \Rightarrow T(\ell) = e^{2\ell}T, \tag{17}$$

$$\frac{dv_3}{d\ell} = v_3 \Rightarrow v_3(\ell) = e^\ell v_3. \tag{18}$$

In general, these flow equations will be corrected once interactions are taken into account, but for the couplings of choice here, the corrections appear only at two-loop order.

To one-loop order, the RG flows of the coupling constants have the form

$$\frac{dg_i}{d\ell} = \sum_{j=1}^{9} \sum_{k=1}^{9} g_j g_k \sum_{a=1}^{4} A_{ijk}^{(a)} \Phi_a \left[v_3(\ell), t(\ell)\right], \qquad (19)$$

where i, like j and k, extends over the aforementioned nine irreducible representations of the groups of the wave vector Γ and $\pm \mathbf{K}$; $A_{ijk}^{(a)}$ are listed in Appendix C. The dimensionless parameters that enter as the arguments of the Φ functions are

$$v_3(\ell) = \frac{v_3(\ell)}{\Lambda/2m^*}, \qquad (20)$$

$$t(\ell) = \frac{T(\ell)}{\Lambda^2/2m^*}. \qquad (21)$$

The Φ functions are determined by the integrals in Eqs. (A4)–(A12). As shown in Appendix A, these integrals can be evaluated explicitly when $v_3 = 0$ in terms of elementary functions or when $t = 0$ in terms of complete elliptic integrals.

In the discussion that follows, we will make use of the asymptotic behavior in the limit of $\ell \to \infty$:

$$\Phi_a \left[v_3(\ell), t(\ell)\right] = \frac{e^{-2\ell}}{2t} + \cdots \quad \text{for} \quad a = 1, 2, \quad (22)$$

$$\Phi_a \left[v_3(\ell), t(\ell)\right] = \frac{e^{-6\ell}}{12t^3} + \cdots \quad \text{for} \quad a = 3, 4, \quad (23)$$

where $t = t(0)$ is the initial dimensionless temperature and "$\cdots$" represent terms that are smaller than the leading terms.

A. General analysis of the RG flows

In general, the flow equations (19) describe two competing tendencies. The term proportional to $g_j g_k$ tends to cause an increase of the absolute value of the coupling constants as ℓ increases, while the Φ functions tend to zero as ℓ increases due to the increase of their arguments $v_3(\ell)$ and $t(\ell)$. Numerical analysis of the flow equations reveals that for fixed values of the initial couplings and for a sufficiently large value of the initial temperature t, there is a certain value of ℓ where the flow becomes stagnant and the coupling constants g tend to *finite* values as $\ell \to \infty$. Therefore if the initial couplings are small, they remain small as long as the initial temperature is sufficiently large even as *all* the modes are integrated out. In this regime, weak-coupling RG is entirely justified. Lowering the initial temperature, while keeping the initial couplings fixed, causes an increase of the value of the RG parameter ℓ where the coupling constants stop flowing and an increase in the limiting value of the coupling constants. At a critical initial temperature t_c, the coupling constants g diverge as $\ell \to \infty$. For an initial temperature $t < t_c$, the coupling constants diverge at finite ℓ.

The role of trigonal warping is to cause additional suppression of the increase of the absolute value of the coupling constants. Thus, for fixed initial values of the coupling constants and for sufficiently large initial v_3, the g's do not diverge even at $t = 0$.

Therefore, as stated previously,[11] for fixed initial v_3, a critical value of the initial coupling(s) must be exceeded for a runaway flow of the coupling constant(s), which we associate with a phase transition, to occur.

In order to understand the nature of the possible ordering tendencies, we first analyze the asymptotic behavior of the equations (19) when $t = t_c > 0$ and $\ell \to \infty$. Provided that at least one coupling g_r diverges, we have managed to enumerate *all* possible solutions for the stable "rays" along which ratios with the other couplings g_j/g_r tend to constants. The detailed analysis of these solutions is given in Sec. III G. Along such a stable ray, all nine differential equations "collapse" onto one, namely,

$$\frac{dg_r}{d\ell} = \mathcal{A}_{(r)} g_r^2 \frac{e^{-2\ell}}{2t_c} + \cdots, \quad \text{as} \quad \ell \to \infty. \qquad (24)$$

Here and in the remainder of the paper, if an index is in parentheses [e.g., (r)], then there is no automatic summation over r unless explicitly stated. The coefficient $\mathcal{A}_{(r)}$ depends on the stable ray along which the couplings diverge and "$\cdots$" denotes terms that vanish faster than $e^{-2\ell}$. Combining the asymptotic behavior of the Φ functions as $\ell \to \infty$, given by Eqs. (19), (22), and (23), the coefficient may be expressed as

$$\mathcal{A}_{(r)} = 2 \sum_{j=1}^{9} \sum_{k=1}^{9} \sum_{a=1}^{2} A_{rjk}^{(a)} \rho_j^{(r)} \rho_k^{(r)}, \qquad (25)$$

where the $\rho_j^{(r)} = g_j/g_r$ is the ratio of two couplings along the stable ray. The solution of differential equation (24) is

$$g_r(\ell) = \frac{4t_c}{\mathcal{A}_{(r)}} e^{2\ell} + \cdots, \quad \text{as} \quad \ell \to \infty, \qquad (26)$$

where "$\cdots$" denotes terms that are smaller than $e^{2\ell}$ as $\ell \to \infty$.

B. Susceptibilities and the nature of the symmetry breaking

To find out what symmetry-breaking tendencies dominate, we start by introducing source terms into our action:

$$\Delta S = \sum_{i=1}^{32} \Delta_i^{\text{ph}} \frac{1}{\beta} \sum_{n=-\infty}^{\infty} \sum_{\mathbf{k}} \psi_{\mathbf{k}}^{\dagger}(\omega_n) O^{(i)} \psi_{\mathbf{k}}(\omega_n)$$

$$+ \frac{1}{2} \sum_{i=1}^{16} \Delta_i^{pp} \frac{1}{\beta} \sum_{n=-\infty}^{\infty} \sum_{\mathbf{k}} \psi_{\mathbf{k}}^{\dagger}(\omega_n) \tilde{O}^{(i)} \psi_{-\mathbf{k}}^{*}(-\omega_n) + \text{c.c.}$$

$$(27)$$

We may think of these terms as "forces" that couple to various observables, which acquire nonzero averages whenever the system enters the appropriate phase. Note that only 18 of the 32 particle-hole source terms introduced are symmetry inequivalent. Similarly, only nine of the 16 particle-particle source terms are inequivalent. The transformation properties of the former under the various symmetry group operations are summarized in Table I. Again, note the absence of explicit spin subscripts on the (eight-component) $\psi = (\psi_\uparrow, \psi_\downarrow)^T$ fields. Terms such as $\psi^\dagger \tilde{O} \psi^*$ should be understood as matrix multiplication, i.e., $\sum_{\alpha,\beta=1}^{8} \psi_\alpha^* \tilde{O}_{\alpha\beta} \psi_\beta^*$. We will see later that only two of the particle-particle, or superconducting, orders can appear, namely the A_{1g} and A_{2u} orders. These correspond

TABLE I. Table of all particle-hole phases considered, listed according to what representation of the D_{3d} point group they transform. The Kekulé and density waves have a wave vector of **K**.

Group rep.	Matrices	Trans.	TRS	Inv.	Mirror refl. (σ_d)	
A_{1g} charge	$1_4 \otimes 1$	$+$	$+$	e	e	Charge instability
A_{2g} charge	$\tau_3\sigma_3 \otimes 1$	$+$	$-$	e	o	Anomalous quantum Hall[37,43]
E_g charge	$(1\sigma_1, \tau_3\sigma_2) \otimes 1$	$+$	$+$	e	e/o	Nematic[11,16]
A_{1u} charge	$\tau_3 1 \otimes 1$	$+$	$-$	o	o	Loop current[44]
A_{2u} charge	$1\sigma_3 \otimes 1$	$+$	$+$	o	e	Layer-polarized[34,36]
E_u charge	$(\tau_3\sigma_1, -1\sigma_2) \otimes 1$	$+$	$-$	o	o/e	Loop current II (ME2)
$A_{1\mathbf{K}}$ (A_{1g}/A_{1u}) charge	$\tau_1\sigma_1 \otimes 1; \tau_2\sigma_1 \otimes 1$	$-$	$+$	e/o	e/o	Kekulé[45]
$A_{2\mathbf{K}}$ (A_{2u}/A_{2g}) charge	$\tau_1\sigma_2 \otimes 1; \tau_2\sigma_2 \otimes 1$	$-$	$-$	o/e	e/o	Kekulé current
$E_{\mathbf{K}}$ (E_g/E_u) charge	$(\tau_1 1, -\tau_2\sigma_3) \otimes 1; (-\tau_2 1, -\tau_1\sigma_3) \otimes 1$	$-$	$+$	e/o	(e/o)/(o/e)	Charge density wave
A_{1g} spin	$1_4 \otimes \vec{\sigma}$	$+$	$-$	e	e	Ferromagnetic
A_{2g} spin	$\tau_3\sigma_3 \otimes \vec{\sigma}$	$+$	$+$	e	o	Quantum spin Hall[15,17,46]
E_g spin	$(1\sigma_1, \tau_3\sigma_2) \otimes \vec{\sigma}$	$+$	$-$	e	e/o	Spin nematic
A_{1u} spin	$\tau_3 1 \otimes \vec{\sigma}$	$+$	$+$	o	o	Staggered spin current
A_{2u} spin	$1\sigma_3 \otimes \vec{\sigma}$	$+$	$-$	o	e	Layer AF[3,12,47]
E_u spin	$(\tau_3\sigma_1, -1\sigma_2) \otimes \vec{\sigma}$	$+$	$+$	o	o/e	Loop spin current II
$A_{1\mathbf{K}}$ (A_{1g}/A_{1u}) spin	$\tau_1\sigma_1 \otimes \vec{\sigma}; \tau_2\sigma_1 \otimes \vec{\sigma}$	$-$	$-$	e/o	e/o	Spin Kekulé
$A_{2\mathbf{K}}$ (A_{2u}/A_{2g}) spin	$\tau_1\sigma_2 \otimes \vec{\sigma}; \tau_2\sigma_2 \otimes \vec{\sigma}$	$-$	$+$	o/e	e/o	Spin Kekulé current
$E_{\mathbf{K}}$ (E_g/E_u) spin	$(\tau_1 1, -\tau_2\sigma_3) \otimes \vec{\sigma}; (-\tau_2 1, -\tau_1\sigma_3) \otimes \vec{\sigma}$	$-$	$-$	e/o	(e/o)/(o/e)	Spin density wave

to s_{++}- and s_{+-}-wave superconducting orders, respectively. Both are s-wave, but the s_{++} order parameter has the same sign on both layers, while the s_{+-} order has opposite signs on each layer. To one-loop order, we find

$$\frac{d \ln \Delta_i^{\text{ph}}}{d\ell} = 2 + \sum_{j=1}^{9} \sum_{a=1}^{4} B_{ij}^{(a)} g_j(\ell) \Phi_a \left[\nu_3(\ell), t(\ell)\right], \quad (28)$$

$$\frac{d \ln \Delta_i^{\text{pp}}}{d\ell} = 2 + \sum_{j=1}^{9} \sum_{a=1}^{4} \tilde{B}_{ij}^{(a)} g_j(\ell) \Phi_a \left[\nu_3(\ell), t(\ell)\right], \quad (29)$$

where the (32×9) matrix $B_{ij}^{(a)}$ and the (16×9) matrix $\tilde{B}_{ij}^{(a)}$ are defined by Eqs. (C29)–(C33) and (C35)–(C36). Note that Eqs. (28) and (29) can be readily integrated, and we find that

$$\Delta_i^{\text{ph/pp}}(\ell) = \Delta_i^{\text{ph/pp}}(0) e^{2\ell} \exp\left[\Omega_i^{\text{ph/pp}}(\ell)\right], \quad (30)$$

where

$$\Omega_i^{\text{ph}}(\ell) = \sum_{j=1}^{9} \sum_{a=1}^{4} B_{ij}^{(a)} \int_0^{\ell} d\ell' \, g_j(\ell') \Phi_a[\nu_3(\ell'), t(\ell')],$$

$$\Omega_i^{\text{pp}}(\ell) = \sum_{j=1}^{9} \sum_{a=1}^{4} \tilde{B}_{ij}^{(a)} \int_0^{\ell} d\ell' \, g_j(\ell') \Phi_a[\nu_3(\ell'), t(\ell')].$$

At $t = t_c > 0$, as $\ell \to \infty$ the $e^{2\ell}$ increase of a divergent coupling g_r exactly balances the $e^{-2\ell}$ decrease of the Φ functions and the right hand sides of the above equations tend to constants,

$$\begin{aligned}
\frac{d \ln \Delta_i^{\text{ph}}}{d\ell} &= 2 + \frac{2\mathcal{B}_{i(r)}^{\text{ph}}}{\mathcal{A}_{(r)}} \quad \text{as } \ell \to \infty, \\
\frac{d \ln \Delta_i^{\text{pp}}}{d\ell} &= 2 + \frac{2\mathcal{B}_{i(r)}^{\text{pp}}}{\mathcal{A}_{(r)}} \quad \text{as} \quad \ell \to \infty.
\end{aligned} \quad (31)$$

In other words, the engineering dimensions of the source terms, which are equal to 2, are corrected by the anomalous

dimensions

$$\eta_i^{\text{ph/pp}} = \frac{2\mathcal{B}_{i(r)}^{\text{ph/pp}}}{\mathcal{A}_{(r)}} \quad (32)$$

due to the electron-electron interactions. Again, in the above equation, there is no summation over r, which corresponds to the divergent coupling g_r that we divided by. The values of the $\mathcal{B}$'s are

$$\mathcal{B}_{i(r)}^{\text{ph}} = 2 \sum_{k=1}^{9} \left(B_{ik}^{(1)} + B_{ik}^{(2)}\right) \rho_k^{(r)}, \quad (33)$$

$$\mathcal{B}_{i(r)}^{\text{pp}} = 2 \sum_{k=1}^{9} \left(\tilde{B}_{ik}^{(1)} + \tilde{B}_{ik}^{(2)}\right) \rho_k^{(r)}, \quad (34)$$

where $B^{(1/2)}$ is given by the sum of Eqs. (C30) and (C32) and $\tilde{B}^{(1/2)}$ is given by Eq. (C35). Note that the expressions for $\mathcal{A}_{(r)}$ and $\mathcal{B}_{(r)}^{\text{ph/pp}}$ depend on the choice of g_r but the $\eta_i^{\text{ph/pp}}$'s do not.

In order to calculate the physical susceptibility toward various ordering tendencies, we calculate the correction to the free energy due to the presence of the symmetry breaking source terms.[48] We find that

$$\begin{aligned}
\delta f(\Delta) &= -\frac{m^*}{16\pi} \sum_{i=1}^{32} \int_0^{\infty} d\ell \, e^{-4\ell} \left[\Delta_i^{\text{ph}}(\ell)\right]^2 \sum_{a=1}^{4} \alpha_{a,i}^{\text{ph}} \Phi_a[\nu_3(\ell), t(\ell)] \\
&\quad -\frac{m^*}{16\pi} \sum_{i=1}^{16} \int_0^{\infty} d\ell \, e^{-4\ell} \left|\Delta_i^{\text{pp}}(\ell)\right|^2 \sum_{a=1}^{4} \alpha_{a,i}^{\text{pp}} \Phi_a[\nu_3(\ell), t(\ell)],
\end{aligned}$$
$$(35)$$

The α coefficients are given in Appendix D by Eqs. (D1)–(D4).

The susceptibilities are then simply given by second derivatives of the free energy with respect to the bare values

of the appropriate source terms,

$$\chi_i^{\text{ph}} = -\frac{\partial^2 f}{\partial\left[\Delta_i^{\text{ph}}(\ell=0)\right]^2}, \tag{36}$$

$$\chi_i^{\text{pp}} = -\frac{\partial^2 f}{\partial\left[\text{Re }\Delta_i^{\text{pp}}(\ell=0)\right]^2} = -\frac{\partial^2 f}{\partial\left[\text{Im }\Delta_i^{\text{pp}}(\ell=0)\right]^2}. \tag{37}$$

Using Eqs. (30) and (35), we find that the susceptibilities given above may be written as

$$\chi_i^{\text{ph/pp}} = \frac{m^*}{8\pi}\sum_{a=1}^{4}\alpha_{a,i}^{\text{ph/pp}}\int_0^\infty d\ell\, e^{2\Omega_i^{\text{ph/pp}}(\ell)}\Phi_a[\nu_3(\ell),t(\ell)]. \tag{38}$$

Note that the source terms, $\Delta_i^{\text{ph/pp}}(\ell=0)$, being auxiliary fields, do not appear.

Any divergence in the susceptibilities has to come from the regions of large ℓ in Eq. (35) where the asymptotic expressions derived earlier hold. Therefore since, for $t = t_c > 0$, the asymptotic behavior of the Φ functions is $e^{-2\ell}$, the condition for the divergence of a susceptibility in a particle-hole or particle-particle channel i is

$$\eta_i^{\text{ph/pp}} > 1. \tag{39}$$

Next, we will relate the anomalous dimensions of the source terms $\eta_i^{\text{ph/pp}}$ to the susceptibility exponents $\gamma_i^{\text{ph/pp}}$.

C. Susceptibility exponents

For $t > t_c$, sufficiently close to t_c the asymptotic behavior of the coupling constants is still approximately described by Eq. (24). If we integrate it from ℓ_0 to ℓ, both of which are asymptotically large (and temperature independent), but not infinite, then we find

$$\frac{1}{g_r(\ell,t)} = \frac{1}{g_r(\ell_0,t)} - \frac{\mathcal{A}_{(r)}}{4t}(e^{-2\ell_0} - e^{-2\ell}). \tag{40}$$

At t_c, we have $1/g_r(\ell_0,t_c) = \mathcal{A}_{(r)}e^{-2\ell_0}/4t_c$ and we can write the above equation as

$$\frac{1}{g_r(\ell,t)} = \left[\frac{1}{g_r(\ell_0,t)} - \frac{1}{g_r(\ell_0,t_c)}\right]$$
$$- \left(\frac{1}{t} - \frac{1}{t_c}\right)\left[\frac{\mathcal{A}_{(r)}}{4}e^{-2\ell_0}\right] + \frac{\mathcal{A}_{(r)}}{4t}e^{-2\ell}. \tag{41}$$

Since ℓ_0 is finite, $g_r(\ell_0,t)$ is analytic in t at t_c and can be expanded as

$$g_r(\ell_0,t) \approx g_r(\ell_0,t_c) + (t-t_c)\frac{\partial}{\partial t}g_r(\ell_0,t)\Big|_{t_c} + \cdots, \tag{42}$$

where "$\cdots$" represents terms of order $(t-t_c)^2$ and higher. Therefore

$$g_r(\ell,t) \approx \frac{1}{c_r(t-t_c) + \frac{\mathcal{A}_{(r)}}{4t}e^{-2\ell}}, \quad \text{as} \quad \ell \to \infty, \quad t \to t_c^+ \tag{43}$$

where

$$c_r = \frac{\partial}{\partial t}\frac{1}{g_r(\ell_0,t)}\Big|_{t_c} + \frac{\mathcal{A}_{(r)}}{4t_c^2}e^{-2\ell_0}. \tag{44}$$

Note that $c_r\mathcal{A}_{(r)} > 0$ since $g_r(\ell_0,t)$ increases in magnitude as $t \to t_c^+$.

The flow of the source terms at large ℓ at $t > t_c$ is determined by substituting the above result into the Eqs. (28) and (29) and taking the asymptotic limit of the Φ functions at large ℓ:

$$\frac{d\ln\Delta_i^{\text{ph}}}{d\ell} = 2 + \frac{\mathcal{B}_{i(r)}^{\text{ph}}}{2t}\frac{e^{-2\ell}}{c_r(t-t_c) + \frac{\mathcal{A}_{(r)}}{4t}e^{-2\ell}}, \tag{45}$$

$$\frac{d\ln\Delta_i^{\text{pp}}}{d\ell} = 2 + \frac{\mathcal{B}_{i(r)}^{\text{pp}}}{2t}\frac{e^{-2\ell}}{c_r(t-t_c) + \frac{\mathcal{A}_{(r)}}{4t}e^{-2\ell}}. \tag{46}$$

Integrating from ℓ_0 to ℓ and substituting to Eq. (35), we find that the singular contribution to the susceptibility for the symmetry breaking source term Δ_i is

$$\chi_i^{\text{ph/pp}} \approx (t-t_c)^{-\gamma_i^{\text{ph/pp}}}, \tag{47}$$

where

$$\gamma_i^{\text{ph/pp}} = \eta_i^{\text{ph/pp}} - 1. \tag{48}$$

Clearly, the susceptibility for a particular order diverges if the condition (39) is satisfied. Note that only if $\eta_i^{\text{ph/pp}} = 2$ do the susceptibility exponents acquire their mean-field values. This is in general not the case here, as will be elaborated on in the next section.

It is also important to stress that these exponents are obtained within the one-loop approximation *of the fermionic theory* and are therefore not expected to be accurate. They are also not expected to be equal to the one-loop exponents obtained within an ϵ expansion of the corresponding bosonic theory, with the Landau functional for the ordering field. The ultimate critical behavior is determined by the universality class of such a bosonic theory. As an example, the finite temperature phase transition into the nematic state belongs to the two dimensional three-state Potts model[11] universality class for which the exponent $\gamma = 13/9$ (see Ref. 49). However, within our one-loop fermionic RG treatment, γ does not exceed $2/3$. Nevertheless, the exponents calculated within the present approximation give us important information about the physical character of the dominant ordering tendency, without any *a priori* bias toward any given order.

Next, we will explicitly calculate the RG flows using numerical integration of the RG equations for the couplings, the symmetry-breaking vertex terms and the physical susceptibilities. We do so for any interaction that can be written as $\sum_{\mathbf{q}}\sum_{i,j}V_{ij}(\mathbf{q})n_i(\mathbf{q})n_j(-\mathbf{q})$, where $V_{ij}(\mathbf{q})$ is finite for any $\mathbf{q}$; i and j run over sublattice and layer indices. To leading order in small V, $\mathbf{q}$ is either near 0 or near $\pm 2\mathbf{K}$. Such a microscopic lattice interaction will initially lead to only three of the nine four-fermion coupling constants in the low-energy effective field theory being finite,[15] i.e., $g_{A_{1g}}|_{\ell=0} \neq 0$, $g_{A_{2u}}|_{\ell=0} \neq 0$, $g_{E_K}|_{\ell=0} \neq 0$.
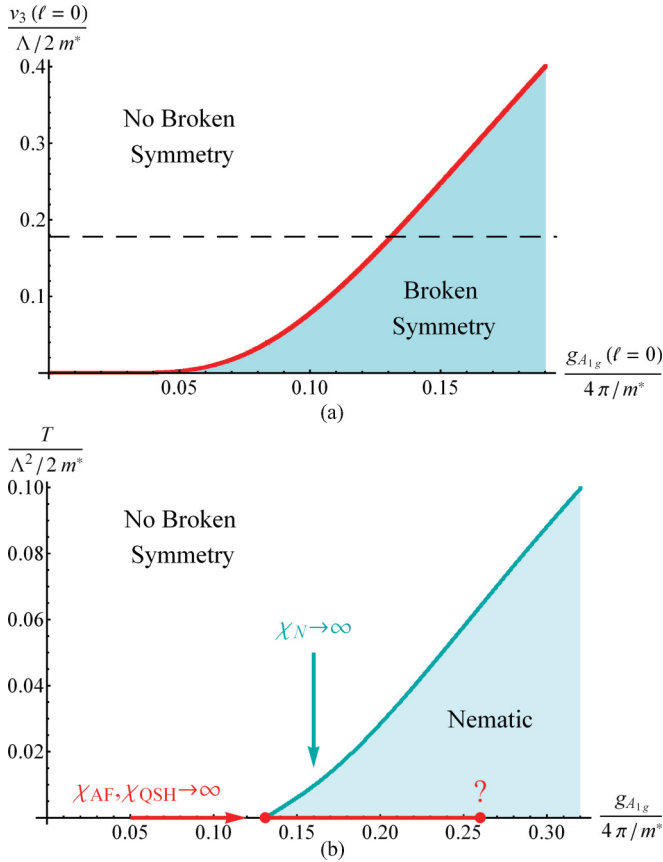
FIG. 2. (Color online) Phase boundaries for bilayer graphene with forward scattering only. (a) At finite trigonal warping, $v_3 = 2m^* v_3 / \Lambda$ and $T = 0$, the bare $g_{A_{1g}}$ must exceed a critical value, given by the red line, in order for the system to enter a broken symmetry phase. Along the dashed line, $v_3 = 0.178$, which is the value used to fit the experimental data in Ref. 6. (b) The transition temperature as a function of the initial value of $g_{A_{1g}}$ at $v_3 = 0.178$. At any finite t_c, the only susceptibility that diverges corresponds to the nematic order parameter (E_g charge), as shown in Fig. 4.

D. Forward scattering limit: nematic

For $V_{ij}(\pm 2\mathbf{K}) = 0$ and equal inter- and intralayer interactions, the only nonzero bare interaction is $g_{A_{1g}}$. Without scattering between the $\mathbf{K}$ and $\mathbf{K}'$ valleys at the microscopic level, no new scattering between them can be generated in the RG flow, Eq. (19). In other words, $g_{A_{1K}}$, $g_{A_{2K}}$, and g_{E_K} remain zero. The only couplings that appear in this case are those in the g and u representations. We studied the problem numerically and present the main results in Figs. 2 and 3.

For any fixed initial v_3, we find that there is a critical value of $g_{A_{1g}}$ below which the weak-coupling RG converges and no phase transition occurs, even at $T = 0$, as shown in Fig. 2(a). In this phase, where no symmetry is broken, there are four Dirac points in the vicinity of each $\mathbf{K}$ point, three of which are anisotropic and one, centered at $\mathbf{K}$ or $\mathbf{K}'$, which is isotropic.

Above the critical value of $g_{A_{1g}}$, the *only* susceptibility that diverges as $t \to t_c^+ > 0$ is toward an electronic nematic, i.e., toward a spin-singlet order parameter that transforms according to the E_g representation (see Table I). We therefore
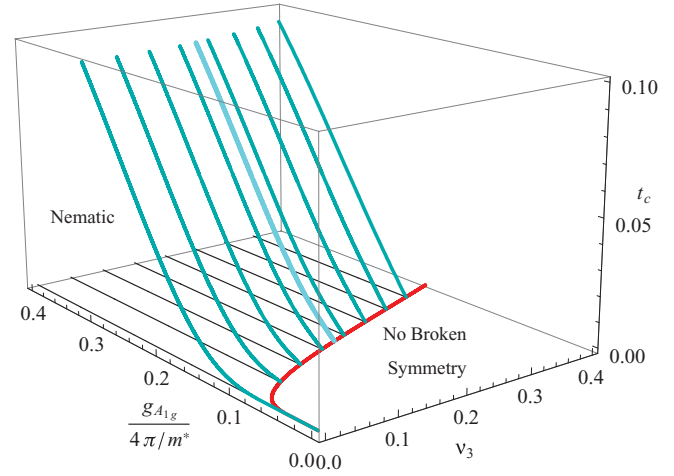

FIG. 3. (Color online) The phase diagram for different values of the forward scattering coupling, $g_{A_{1g}}$, trigonal warping velocity, $v_3 = 2m^* v_3 / \Lambda$, and temperature $t = 2m^* T / \Lambda^2$. At any finite t_c and at any value of v_3 the nematic susceptibility is the only one that diverges. The lighter cyan line, also shown in Fig. 2(b), corresponds to $v_3 = 0.178$, which is the value used throughout the paper.

conclude that, immediately below this temperature, the system enters this symmetry-breaking phase. In Ref. 6, the experimental data is fitted using a value of the trigonal warping velocity corresponding to our dimensionless parameter $v_3 = 0.178$. Here and in the remainder of the paper, we use this value. The phase boundary for that particular choice of v_3 is shown in Fig. 2(b). In Fig. 4, we show the susceptibilities as a function of temperature for various order parameters. This plot corresponds to the vertical arrow in Fig. 2(b) where only the nematic susceptibility diverges. We find that the susceptibility toward the nematic order parameter, despite being smaller than the others at large T, outgrows all competing susceptibilities as the temperature is lowered toward T_c, and is the only susceptibility to diverge at T_c.
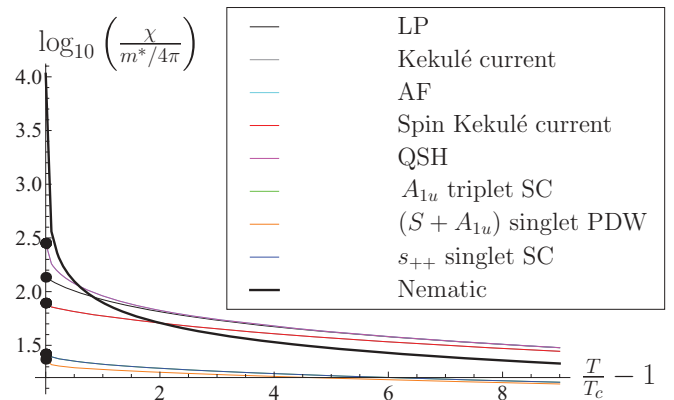

FIG. 4. (Color online) Various susceptibilities calculated from the free energy given by Eq. (35) with forward scattering only. Although the nematic susceptibility is lower than the others at higher temperatures, it is the only susceptibility that diverges as the temperature is lowered towards $t_c > 0$. Here, $v_3 = 0.178$, the bare couplings are $g_{A_{1g}} = 0.161 \times 4\pi/m^*$, and all others zero. In this case, $t_c = 0.01$.

While our analysis of the susceptibilities reveals that at $t_c > 0$ only the nematic susceptibility diverges for any fixed ν_3, this susceptibility does not diverge when approaching the critical $g_{A_{1g}}$ from below exactly at $t = 0$. Instead, we find that the susceptibilities for the layer antiferromagnet (AF) and quantum spin Hall (QSH) order parameters diverge with equal exponents. This suggests that, for $0 < t < t_c$, the system orders into a nematic state, while, at $t = 0$, there may be a coexistence of this state with AF and/or QSH.[50] The complete phase diagram for different values of $g_{A_{1g}}$, ν_3, and t_c is shown in Fig. 3. For the entire range of ν_3's shown, we always find the nematic as the leading instability at finite temperature.

In order to facilitate the comparison with the previous work, which also deals with the forward scattering limit at $T = \nu_3 = 0$, we first note that the three couplings g_1, g_2, and g_3 in Ref. 11 correspond to $g_{A_{1g}}$, $g_{A_{2g}}$, and $g_{E_{2g}}$, respectively. Because $\nu_3 = 0$, none of the other nine four fermion couplings are generated under RG. The "susceptibilities" calculated therein correspond to the logarithmic prefactors on the right-hand sides of Eqs. (15) and (16) in Ref. 11, and are analogous to the more general expressions in Eqs. (28) and (29) of this publication. The physical susceptibilites, considered in this paper, can be straightforwardly obtained from such expressions by substituting the flow of the source terms into the formula (35). At $T = 0$, the divergences appear at finite $\ell = \ell^*$, which can be set as the upper limit on the integrals in Eq. (35). The coupling constant ratio[11] $g_{A_{1g}}/g_{E_g} \to 0$ as $\ell \to \ell^*$. The ratio $g_{A_{2g}}/g_{E_g}$ can approach either $m_1 \approx -0.525$ or $m_3 \approx 13.98$, i.e., the minimal or the maximal root of the cubic equation $(x - 14)x^2 + 4 = 0$.

The analysis of the physical susceptibilities for the conditions stated in Ref. 11 reveals that, as $\ell \to \ell^*$, the *only* physical susceptibility that diverges when $g_{A_{2g}}/g_{E_g} \to m_1$ is towards the nematic; the others remain finite at ℓ^*. Similarly, the *only* susceptibility that diverges when $g_{A_{2g}}/g_{E_g} \to m_3$ is toward the quantum anomalous Hall state (QAH). Very recently, Fan Zhang *et al.* posted a preprint[51] in which they recovered the $T = \nu_3 = 0$ flow equations for the three couplings in Ref. 11. Under equivalent conditions to those in Ref. 11, they claim to have calculated susceptibilities and that the "strongest divergence occurs for the flavor spin channel broken inversion symmetry." These results are at odds with our findings. We believe the discrepancy to originate from their Eq. (C24), which does not properly account for renormalization of composite operators (see Refs. 52 and 53).

E. General density-density interaction

In the previous section, we have shown how a system with forward scattering only at the bare level orders into the nematic state at any finite temperature. In general, however, other four-fermion coupling constants may be nonzero as well. In a previous work on this subject,[15] two of us showed how to find the bare interaction strengths corresponding to a screened interaction in the weak coupling limit. In addition to $g_{A_{1g}}$, two other couplings, $g_{A_{2u}}$ and g_{E_K}, appear at $\ell = 0$. Due to the presence of these couplings, all β functions are nonzero and all nine couplings allowed by symmetry are generated in the RG flow.

Instead of seeking a critical temperature for a given set of initial couplings, we invert the procedure by fixing the transition temperature to $t_c = 0.01$. This value is in accordance with the experimentally observed symmetry-breaking energy scale of ~ 2 meV. We then determine what values of the initial couplings would make the RG flow divergent at this temperature. This set of points defines a two-dimensional surface in the three-dimensional space of initial $(g_{A_{1g}}, g_{A_{2u}}, g_{E_K})$. For each point on this surface, we find the list of phases for which the susceptibility divergence criterion, Eq. (39), is satisfied. For certain initial conditions, it happens that two or more susceptibilities diverge at t_c. In such situations, we list all the phases with diverging susceptibilities (e.g., "N + AF" represents the region of initial couplings where both χ_N and χ_{AF} diverge, although not necessarily with the same exponent). Because our formalism is valid only for $t \geqslant t_c$, the resulting state may be either one of the listed phases or a coexistence of several of these phases. In order to decide which phase(s) is present, one needs to construct a theory valid below t_c, such as a Landau theory with multiple order parameters. This is beyond the scope of the present paper.

The phase diagram we find is presented in Fig. 5. One should understand the axes on this plot as follows. When the microscopic interaction has a long range, the bare values of
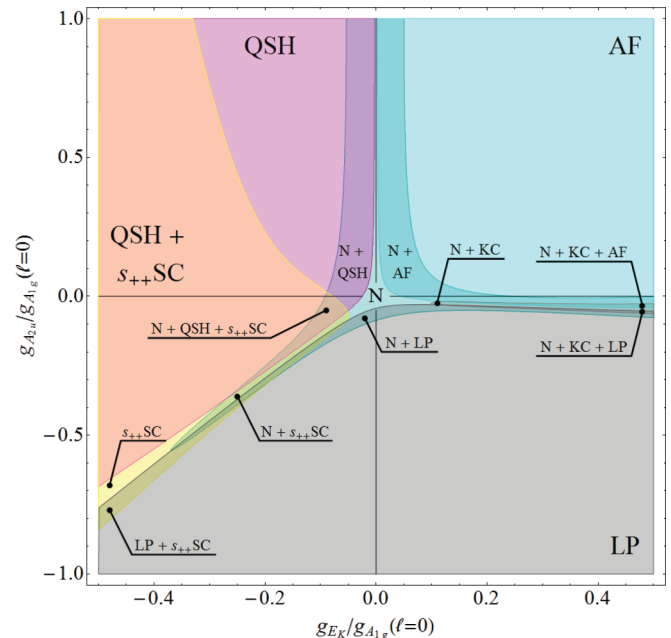

FIG. 5. (Color online) The phase diagram of bilayer graphene with trigonal warping. The transition temperature is fixed to $t_c = 0.01$ and $\nu_3 = 0.178$. Predominantly forward scattering favors the nematic (N) phase. When backscattering and/or the difference between inter- and intralayer scattering is considerable at the bare level we find other phases: the layer antiferromagnet (AF), the layer-polarized state (LP), the quantum spin Hall state (QSH), the s_{++} superconducting state (s_{++} SC), and the Kekulé current state (KC). In regions where two or more susceptibilities diverge at the same t_c we use "$+$" to denote a "coexistence" of multiple possible phases. Whether the listed phases truly coexist or one of them is preferred must be determined from the full Landau function. Such an analysis is beyond the scope of this paper.

$g_{A_{2u}}$ and $g_{E_\mathbf{K}}$ are negligible relative to $g_{A_{1g}}$. They become larger for interactions with shorter range.[15] For monotonically decreasing repulsive interaction potentials, these two couplings do not exceed $g_{A_{1g}}$ and $g_{A_{1g}}/2$, respectively. $g_{A_{2u}}$ and $g_{E_\mathbf{K}}$ reach these values in the Hubbard limit, where the only microscopic interaction term is on-site. We therefore restrict our phase diagram to positive initial values of $g_{A_{1g}}$, to $|g_{E_\mathbf{K}}|/g_{A_{1g}} \leqslant 1/2$, and to $|g_{A_{2u}}|/g_{A_{1g}} \leqslant 1$.

In the given range of initial couplings, we find a rich phase diagram with the following phases:

(a) Nematic (N): this phase is stable for predominantly forward scattering, i.e., when both $g_{A_{2u}}$ and $g_{E_\mathbf{K}}$ are small at the bare level. If one of these couplings remains small and the other becomes comparable to $g_{A_{1g}}$ the nematic susceptibility is still divergent, although other susceptibilities will diverge at these initial values as well. The nematic state is gapless, but it reconstructs the low-energy spectrum such that two out of four Dirac cones in each valley become gapped.

(b) Layer antiferromagnet (AF): this phase occurs when all three bare couplings are repulsive and comparable, corresponding to a short-range repulsive interaction. In this state, the magnetization on each undimerized site is finite, with the magnetization within one layer pointing in one direction, and that in the other layer in the opposite direction.

(c) Layer-polarized state (LP): this phase is preferred when the interlayer repulsion is stronger than the intralayer repulsion [$g_{A_{2u}}(\ell = 0) \lesssim 0$], and the backscattering is either repulsive or weakly attractive [$g_{E_\mathbf{K}}(\ell = 0) \gtrsim g_{A_{2u}}(\ell = 0)$]. In this phase, which is gapped, there is an imbalance of the electron occupation number between the two layers. One layer is more occupied and the opposite layer is equally less occupied with respect to the symmetric, high-temperature state.

(d) Quantum spin Hall state (QSH): this state is preferred when the backscattering is attractive [$g_{E_\mathbf{K}}(\ell = 0) \lesssim 0$], but if $g_{A_{2u}}$ is attractive as well, it must be weaker [$g_{E_\mathbf{K}}(\ell = 0) \lesssim g_{A_{2u}}(\ell = 0)$]. In this state, which is gapped, there is a spin current around each plaquette circulating in the same direction in both layers.

(e) s_{++} superconductor (s_{++} SC): the conditions for this phase are similar to the previous one in that the backscattering must be attractive, but it must also be roughly stronger than (attractive or repulsive) $|g_{A_{2u}}|$ at $\ell = 0$. This state opens a superconducting gap in both layers with the same sign on each layer.

(f) Kekulé current phase (KC): this phase appears in a thin sliver of initial couplings for which backscattering is repulsive and comparable to $g_{A_{1g}}$, while the inter- and intralayer couplings are roughly the same [$g_{A_{2u}}(\ell = 0) \approx 0$]. It breaks lattice translational symmetry and time-reversal symmetry. In this phase a supercell, consisting of three regular unit cells, is formed. Within the supercell, two plaquettes carry a circulating current, both in the same direction. This phase is gapped.

For a graphical illustration of some of these phases, see Fig. 2 in Ref. 17.

In the entire plot, the values of the bare dimensionless couplings $m^* g_i/4\pi$ for which the system orders at the preset $t_c = 0.01$ and $\nu_3 = 0.178$ are always smaller than 0.15, which justifies our weak-coupling approach. The situation does not change qualitatively with variations in temperature or in the absence of trigonal warping—we explored a range of temperatures $0.005 \leqslant t_c \leqslant 0.02$ with and without trigonal warping and found that the general structure of the phase diagram in Fig. 5 does not change appreciably. This is not a coincidence and, later in the paper, we will map the phases that we may obtain by analyzing the behavior of the flow equations in the large ℓ limit, where trigonal warping is irrelevant.

F. The Hubbard model—"hidden" symmetry

As an important check, we apply our RG procedure to a special case, namely the Hubbard model, about which we already know certain exact properties. At half-filling, this model has a dynamical SO(4) symmetry[28] on a bipartite lattice. This symmetry is present regardless of the sign of U and the dimensionality. When U is negative, this symmetry is particularly useful because the electrons have a tendency toward pairing. One good variational ground state for the negative U Hubbard model on a square lattice is a charge density wave, where one sublattice has a higher occupation number than the other. Another ground state that exhibits pairing is the s-wave superconductor. The pseudospin symmetry rotates between these states. At half-filling, the tendency towards the charge density wave order must therefore be the same as the tendency towards the s-wave superconducting order.

In the case of bilayer graphene, the nomenclature is slightly different. A difference in the number of electrons in one sublattice compared to the other corresponds to a layer-polarized state and not to a CDW because the layer-polarized state does not break the translational symmetry of the lattice. Among a plethora of superconducting orders in bilayer graphene, the one that is obtained by pseudospin rotation from the layer-polarized state is the s_{++} superconductor. Following the argument in the previous paragraph, we conclude that the tendencies towards the layer-polarized and s_{++} superconducting orders are exactly the same in bilayer graphene at half filling with an attractive Hubbard interaction.

In addition, a repulsive Hubbard model is related to its attractive counter part with an equally strong interaction. The mapping between the two is given by[29]

$$c_\uparrow(\mathbf{R}) \to \tilde{c}_\uparrow(\mathbf{R}), \qquad (49)$$

$$c_\downarrow(\mathbf{R}) \to (-1)^\mathbf{R} \tilde{c}_\downarrow^\dagger(\mathbf{R}). \qquad (50)$$

It is easy to demonstrate that, under these transformations, the kinetic term of a Hubbard model on a bipartite lattice at half filling remains the same, while the interaction term changes sign.

The pseudospin symmetry, as well as the mapping of the repulsive Hubbard model to its attractive counterpart, are also present in the honeycomb bilayer lattice. The question is then whether any of these properties survive in the low-energy effective field theory, in which the only degrees of freedom considered are those around $\mathbf{K}$ and $\mathbf{K}'$. In the β functions, Eq. (19), the pseudospin symmetry is not apparent. Moreover, once we start from a set of bare interactions corresponding to the Hubbard interaction, all nine couplings are generated. However, as we will now demonstrate, both the pseudospin

symmetry and the connection between the attractive and repulsive Hubbard models are present in the RG flow. These manifest themselves through certain linear combinations of the couplings that are invariant when the bare interactions correspond to the Hubbard model.

We start by rewriting the mapping given by Eqs. (49) and (50) for our low-energy effective theory. Fields with spin up transform as

$$\psi^{(b1/b2)}_{\pm\mathbf{K}\uparrow}(\mathbf{q}) \rightarrow \tilde{\psi}^{(b1/b2)}_{\pm\mathbf{K}\uparrow}(\mathbf{q}),\tag{51}$$

while those with spin down transform according to

$$\psi^{(b1)}_{\pm\mathbf{K}\downarrow}(\mathbf{q}) \rightarrow \tilde{\psi}^{(b1)*}_{\mp\mathbf{K}\downarrow}(-\mathbf{q}),\tag{52}$$

$$\psi^{(b2)}_{\pm\mathbf{K}\downarrow}(\mathbf{q}) \rightarrow -\tilde{\psi}^{(b2)*}_{\mp\mathbf{K}\downarrow}(-\mathbf{q}).\tag{53}$$

This mapping leaves the kinetic term, Eq. (5), invariant, as it should, but it changes the interaction term, Eq. (12),

$$\frac{1}{2}\sum_S g_S(\psi^\dagger S\psi)^2 \rightarrow \frac{1}{2}\sum_S \tilde{g}_S(\tilde{\psi}^\dagger S\tilde{\psi})^2,\tag{54}$$

where each coupling constant $\tilde{g}_S$ is a linear combination of the coupling constants g_S before the transformation. We find that four of the nine coupling constants, $g_{A_{2g}}$, g_{E_g}, $g_{A_{1u}}$, and $g_{A_{1\mathbf{K}}}$, do not change sign, i.e., $g_i \rightarrow \tilde{g}_i$, under this mapping. We call these coupling constants "even." In addition, there are two linear combinations:

$$g_a = g_{A_{1g}} + g_{A_{2u}} + \tfrac{1}{2}g_{E_\mathbf{K}},\tag{55}$$

$$g_b = g_{A_{1g}} - g_{A_{2u}} + g_{E_u} + g_{A_{2\mathbf{K}}},\tag{56}$$

which change sign under the mapping, i.e., $g_{a/b} \rightarrow -\tilde{g}_{a/b}$. We will refer to these as "odd." Finally, there are three remaining linearly independent combinations of the coupling constants:

$$\delta g_1 = g_{A_{1g}} - g_{A_{2u}} - 2g_{E_u},\tag{57}$$

$$\delta g_2 = g_{A_{1g}} - g_{A_{2u}} - 2g_{A_{2\mathbf{K}}},\tag{58}$$

$$\delta g_3 = g_{A_{1g}} + g_{A_{2u}} - 4g_{E_\mathbf{K}},\tag{59}$$

which are neither "even" nor "odd," as they generate terms proportional to themselves as well as terms proportional to "even" and "odd" coupling constants in the RG flow. Clearly, a nonzero value of any δg_i would spoil the connection between the two models.

In the Hubbard limit, we notice that all three δg_i's are zero at $\ell = 0$. We also see that, initially, all other couplings are exactly zero except for $g_a \sim 9U/4 \neq 0$. Therefore Eqs. (51)–(53), when applied to a repulsive Hubbard model with interaction strength U, changes the sign of the only nonzero coupling $\tilde{g}_a = -g_a$ and leaves all the other couplings zero. This is precisely the bare interaction of an attractive Hubbard model with the same interaction strength.

So far, we have shown that the low-energy effective field theories for the repulsive and attractive Hubbard models in bilayer graphene map onto each other, but only at the bare level. To show the equivalence at any ℓ, we look at the flow of the coupling constants, i.e., their linear combinations, Eqs. (55)–

(59). For the three couplings, Eqs. (57)–(59), we find that

$$\frac{d\delta g_i}{d\ell} = \beta_{\delta g_i}(\delta g_1, \delta g_2, \delta g_3) \xrightarrow{\delta g_j \rightarrow 0} 0.\tag{60}$$

The last arrow means that all three β functions vanish when all three δg_i's are simultaneously zero. Since this is true at $\ell = 0$ in the Hubbard limit, it follows that no δg_i's can be generated in the RG flow.

On the other hand, the "even" and "odd" coupling constants *do* flow under RG, but there is a special structure to their β functions. The four "even" couplings flow according to

$$\frac{dg_i^{(e)}}{d\ell} = \sum_{a=1}^4 \left[\sum_{j,k=1}^4 g_j^{(e)}g_k^{(e)}\bar{A}_{ijk}^{(e/e)(a)} \right.$$
$$\left. + \sum_{j,k=1}^2 g_j^{(o)}g_k^{(o)}\bar{A}_{ijk}^{(o/o)(a)} \right]\Phi_a.\tag{61}$$

The flows of the two "odd" couplings are given by

$$\frac{dg_i^{(o)}}{d\ell} = 2\sum_{a=1}^4 \sum_{j=1}^2 \sum_{k=1}^4 g_j^{(o)}g_k^{(e)}\bar{A}_{ijk}^{(o/e)(a)}\Phi_a.\tag{62}$$

The fact that all δg_i's are zero for any ℓ has already been incorporated, and thus there are only six independent couplings. The structure of Eqs. (61) and (62) makes them manifestly invariant under the transformation (51)–(53). Therefore an RG flow obtained within the continuum low-energy effective field theory corresponding to an attractive Hubbard model is described by the same set of differential equations as its repulsive counterpart. The flows of the "even" couplings are identical for the two cases, while those for the "odd" couplings differ only by a sign. The three couplings δg_i are all zero at any ℓ for both cases. Had the flow started from a point where at least one of the δg_i's were finite, this correspondence would have been spoiled because additional terms appear in Eqs. (61) and (62).

An immediate consequence of the mapping described here is that physical quantities obtained in our one-loop RG method for a repulsive Hubbard model are related to those obtained from its attractive counterpart. For example, the "critical temperatures" t_c for the two models are the same. Of course, the layer antiferromagnetic phase for the repulsive Hubbard model and the layer-polarized and s_{++} superconducting phases for the attractive Hubbard model both have the zero transition temperature because a continuous $O(3)$ symmetry cannot be broken at any finite temperature in two dimensions. The finite t_c that we obtain within this approximate technique corresponds to a gap scale that must be the same for both models.

Having demonstrated these special properties of the RG flow in the Hubbard limit, we now compare the susceptibilities for the layer-polarized and s_{++} superconducting states. The α coefficients for the corresponding source terms in the free energy, Eq. (35), are equal. Therefore it is sufficient to look at the difference of the right-hand sides of Eqs. (28)
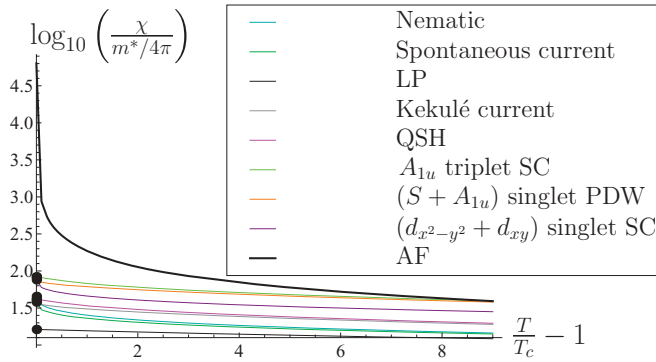
FIG. 6. (Color online) Susceptibilities for the repulsive Hubbard model on the honeycomb bilayer. The AF susceptibility is the most dominant at all temperatures. The dominance of the AF susceptibility over the others is a sign of growing AF correlations. Here, $\nu_3 = 0.178$, the bare couplings are $g_{A_{1g}} = g_{A_{2u}} = g_{E_\mathbf{K}} = 0.0560 \times 4\pi/m^*$, and all others zero. In this case, $t_c = 0.01$.

and (29):

$$\frac{d \ln \Delta_{\mathrm{LP}}}{d\ell} - \frac{d \ln \Delta_{s_{++}}^{\mathrm{SC}}}{d\ell}$$
$$= 2 \left(g_{A_{1g}} - 3g_{A_{2u}} - 2g_{E_u} - 2g_{A_{2\mathbf{K}}} + 4g_{E_\mathbf{K}} \right) (\Phi_1 + \Phi_4)$$
$$= 2 \left(\delta g_1 + \delta g_2 - \delta g_3 \right) (\Phi_1 + \Phi_4) \xrightarrow{\delta g_j \to 0} 0. \quad (63)$$

Since none of the δg_i's are generated in the RG flow in the Hubbard limit, the source terms for the layer-polarized and s_{++} superconducting states flow in exactly the same way, their susceptibilities must diverge with the same exponent. This proves that our one-loop RG treatment respects the pseudospin symmetry of the Hubbard model at half-filling. This argument remains valid for any value of the trigonal warping, which does not break particle-hole symmetry, since no assumptions were made about Φ functions.

Notice that the Hubbard limit is not the only case in which the mapping and consequent pseudospin symmetry are realized. Any model in which the bare values of all three δg_i's are simultaneously zero will exhibit the above correspondence as well. However, if we restrict ourselves to microscopic density-density interaction Hamiltonians, in which case only three of the four-fermion coupling constants are initially nonzero, the pseudospin symmetry is present only if $g_{A_{1g}} = g_{A_{2u}} = 2g_{E_\mathbf{K}}$.

At the end of this section we present numerically obtained susceptibilities for various orders in the case when $g_{A_{1g}} = g_{A_{2u}} = 2g_{E_\mathbf{K}}$. In Fig. 6, susceptibilities to various orders in the repulsive Hubbard model are shown as functions of temperature. The AF susceptibility dominates and is the only one to diverge at T_c. Reiterating what was stated before, this divergence is an artifact of our one-loop RG approximation. Nevertheless, one-loop RG correctly singles out the state that is known to be the ground state at $T = 0$. The t_c that we find should be thought of as a gap scale for the AF order. Figures 7 and 8 compare the layer-polarized and s_{++} superconducting susceptibilities. In Fig. 7, an attractive Hubbard model is studied. In Fig. 8, we consider the same model with an additional small b_1-b_2 repulsion (left) or attraction (right). This additional term violates the pseudospin
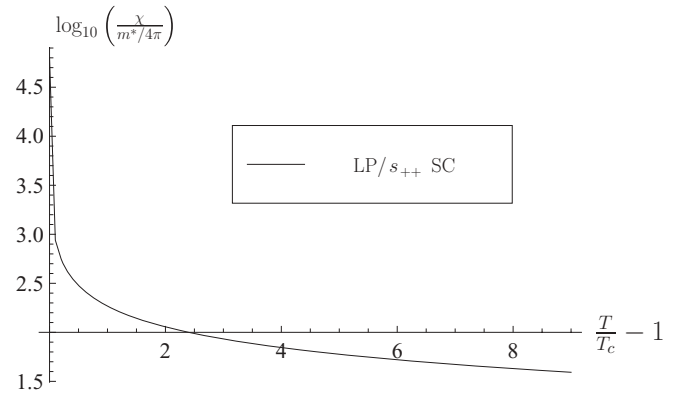

FIG. 7. Susceptibilities toward the layer-polarized and s_{++} superconducting orders in the attractive Hubbard model. In this case, both susceptibilities are equal. The bare coupling constants used here are $g_{A_{1g}} = g_{A_{2u}} = 2g_{E_\mathbf{K}} = -0.0560 \times 4\pi/m^*$, with all others zero. The transition temperature in this case is $t_c = 0.01$.

symmetry of the Hubbard Hamiltonian. In this case, the coupling constants are the same as in the Hubbard model, except that now $g_{A_{2u}} = \frac{1-\epsilon}{1+\epsilon} g_{A_{1g}}$, where $\epsilon = V/U$ and V is the microscopic b_1-b_2 interaction strength. When this interaction is repulsive, the system favors the layer-polarized state over the superconducting state analogous to, for example, the findings of Ref. 33. Conversely, when this interaction is attractive, it favors delocalization of the electron pairs and the concomitant superconducting ground state. Our numerical results are in the agreement this.

G. Fixed ratios and broken symmetry phases

The list of phases found numerically in the previous section shows ordering trends for bilayer graphene only for a certain kind of microscopic interaction that we believe is relevant in a realistic system. The question is whether there are other possible ordered states in bilayer graphene when all nine symmetry-allowed couplings are included at $\ell = 0$. One way to answer this question is to numerically explore the entire nine-dimensional space of bare couplings for various trigonal warping parameters. Such an approach, although straightforward, would require immense computational power and might even miss certain phases that are realized only for specific bare interactions. Fortunately, there is another approach to the problem that we discuss in this section. Instead of concentrating on the bare interactions, we look at what happens to the couplings and susceptibilities at large ℓ. This allows us to enumerate all the possible phases regardless of the initial interactions.

Previously, we discussed the asymptotic behavior of the RG equations at $t = t_c > 0$. We know that at least one coupling will diverge as $g_r(\ell) \sim e^{2\ell}$. We divide all the other couplings by that particular coupling and find the β functions for the ratios, $\rho_j^{(r)} = g_j/g_r$, to be

$$\frac{d\rho_j^{(r)}}{d\ell} = \frac{\dot{g}_j g_r - \dot{g}_r g_j}{g_r^2} = g_r(\ell) \sum_{k,l} \rho_k^{(r)} \rho_l^{(r)}$$
$$\times \sum_{a=1}^4 \left[A_{jkl}^{(a)} - A_{rkl}^{(a)} \rho_j^{(r)} \right] \Phi_a[\nu_3(\ell), t(\ell)]. \quad (64)$$
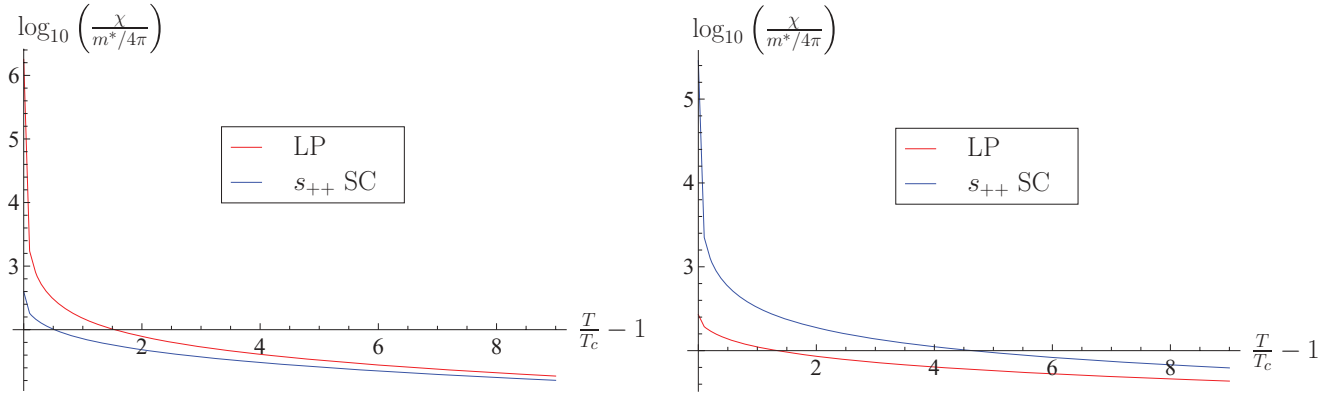
FIG. 8. (Color online) Comparison of the susceptibilities for the layer-polarized and s_{++} superconducting orders in the attractive Hubbard model with an additional small b_1-b_2 interaction. In this case, $g_{A_{2u}} = \frac{1-\epsilon}{1+\epsilon} g_{A_{1g}}$, where $\epsilon = V/U$ and V is the microscopic b_1-b_2 interaction strength. In both cases, the bare $g_{A_{1g}} = 2g_{E_K} = -0.0560 \times 4\pi/m^*$. (Left) When a small b_1-b_2 repulsion is added, the layer-polarized state is preferred. Its susceptibility diverges at t_c, while that of the superconducting state, as well as all other order parameters considered, reaches a finite value. Here, we take $\epsilon = 0.1$, in which case $t_c = 5.18 \times 10^{-3}$. (Right) In the case of a small b_1-b_2 attraction, the opposite is true—the susceptibility for the s_{++} superconducting state diverges, while that for the layer-polarized state remains finite at t_c. Here, $\epsilon = -0.1$ in which case $t_c = 0.0288$.

Here, a dot over a coupling constant represents a derivative with respect to ℓ. In the large ℓ limit, these equations become

$$\dot{\rho}_j^{(r)} = \frac{8t_c}{\mathcal{A}_{(r)}} \sum_{k,l} \rho_k^{(r)} \rho_l^{(r)} \sum_{a=1}^{2} \left[A_{jkl}^{(a)} - A_{rkl}^{(a)} \rho_j \right]. \quad (65)$$

We now ask if these equations have any fixed points, or, in our terminology, "fixed rays." These are obtained by demanding that the right hand sides of all eight equations (65) are simultaneously equal to zero. After finding the fixed rays, we need to determine whether each ray is stable, unstable, or mixed by analyzing eigenvalues of the stability matrix $S_{jk} = \partial \dot{\rho}_j^{(r)}/\partial \rho_k^{(r)}$. Since $\mathcal{A}_{(r)}$ is already defined in Eq. (25) in terms of the ratios, the entire stability matrix has well-defined eigenvalues for each "fixed ray" solution. In addition, the sign of $\mathcal{A}_{(r)}$ determines the sign of the diverging coupling that we divide the others by; see Eq. (24).

If we find that a ray is stable, then, if we start with the coupling constants sufficiently close to the fixed ray, then the ratios of the couplings approach the given set of values as $\ell \to \infty$. Such a flow leads to a divergent susceptibility in at least one channel. If a ray is mixed or unstable, then, in the absence of fine-tuning, the RG flow cannot take the couplings toward such a ratio; even if the flow starts in such a direction for small ℓ, it will be redirected toward some other ray that is stable. We therefore conclude that all the solutions that have even one positive eigenvalue in their stability matrix are physically irrelevant. It is possible that some rays are marginal in certain directions, meaning that some of the eigenvalues of the stability matrix are zero, and stable in others. We do, in fact, find such physically relevant solutions.

Following the procedure described above for all possible choices of the divergent coupling, we find that the stable solutions of the RG flow are situated either on a manifold that we call the "target plane" or on one of four isolated fixed rays. The "target plane" represents a set of stable rays that are marginal in two directions and stable in six others. The target plane and the phases corresponding to each point within are shown in Fig. 9.

We parametrize the plane in the following way. We choose as our parameters the following two coupling constant ratios:

$$x = \lim_{\ell \to \infty} \frac{g_{E_u}}{g_{E_g}}\bigg|_{t=t_c}, \quad (66)$$

$$y = \lim_{\ell \to \infty} \frac{g_{E_K}}{g_{E_g}}\bigg|_{t=t_c}. \quad (67)$$

Since, for certain fixed rays, g_{E_u} and/or g_{E_K} diverge, while g_{E_g} does not, these parameters take values in the interval $(-\infty, \infty)$, including infinite values. With the chosen parametrization, we express each coupling at large ℓ as

$$\frac{g_{A_{1g}}}{G(\ell)}\bigg|_{t=t_c} = 0, \quad g_{A_{2g}}\big|_{t=t_c} = \frac{(1+x+2y)^2}{C(x,y)}G(\ell),$$

$$g_{E_g}\big|_{t=t_c} = \frac{-2(1+x+2y)}{C(x,y)}G(\ell), \quad (68)$$

$$g_{A_{1u}}\big|_{t=t_c} = \frac{4y^2}{C(x,y)}G(\ell), \quad g_{A_{2u}}\big|_{t=t_c} = \frac{4x}{C(x,y)}G(\ell),$$

$$g_{E_u}\big|_{t=t_c} = \frac{-2x(1+x+2y)}{C(x,y)}G(\ell), \quad (69)$$

$$g_{A_{1K}}\big|_{t=t_c} = \frac{4xy}{C(x,y)}G(\ell), \quad g_{A_{2K}}\big|_{t=t_c} = \frac{4y}{C(x,y)}G(\ell),$$

$$g_{E_K}\big|_{t=t_c} = \frac{-2y(1+x+2y)}{C(x,y)}G(\ell), \quad (70)$$

where $C(x,y)$ is a square root of a quartic polynomial and the "overall" coupling $G(\ell) = [\sum_{j=1}^{9} g_j^2]^{1/2}$ is a *positive definite* function of ℓ that diverges as $\ell \to \infty$. The expression for $C(x,y)$ can be readily obtained from the definition of $G(\ell)$, but is unwieldy, and thus we do not include it here. The ratios of any two couplings at large ℓ depend only on x and y, although sometimes these ratios may be infinite.

In the special situation in which the parameters x and y are infinite, but their ratio is finite, we may reparameterize x and y as $x = R\cos\eta$ and $y = R\sin\eta$ and take the limit as $R \to \infty$. The only diverging couplings in this case are $g_{A_{2g}}, g_{A_{1u}}, g_{E_u}, g_{A_{1K}}$, and g_{E_K}. Note that, for each η, we obtain the same stable
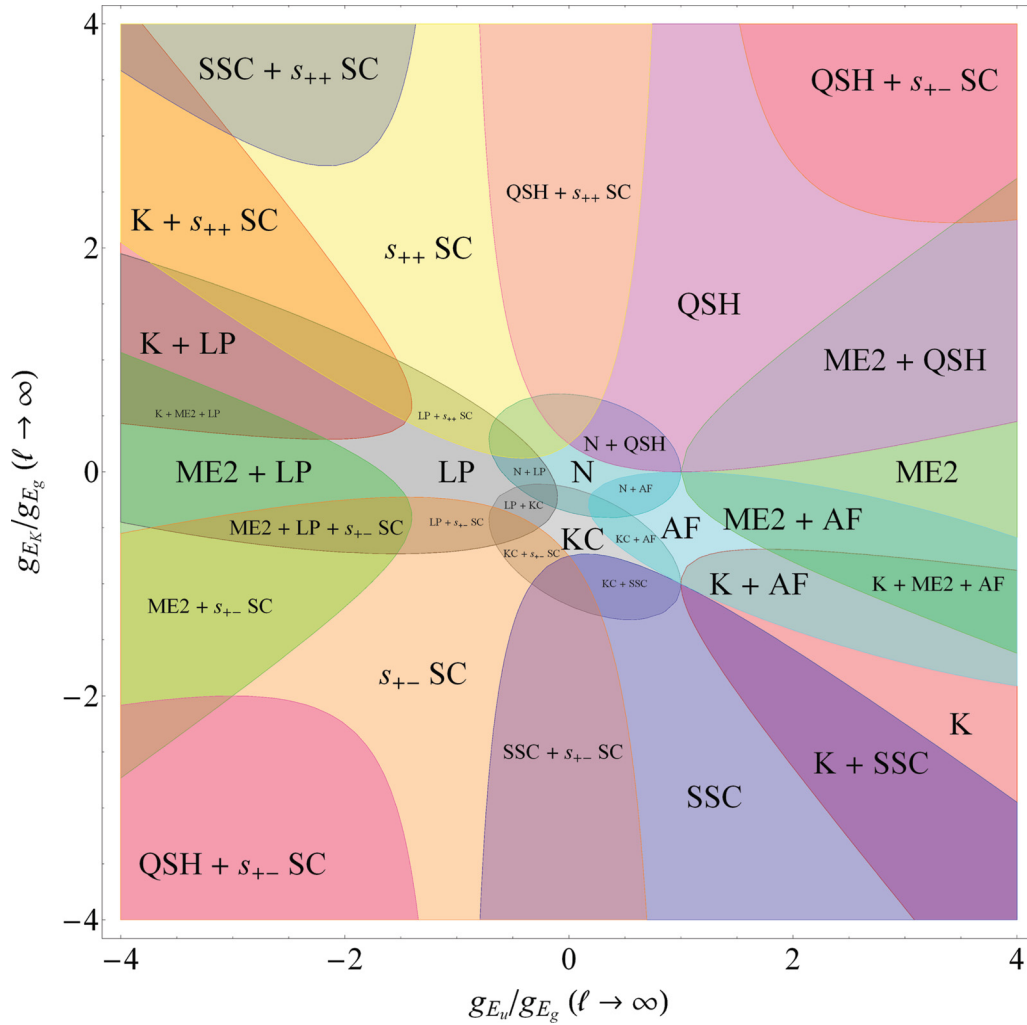
FIG. 9. (Color online) A plot of all of the phases found in the fixed plane described by Eqs. (68)–(70). We find nematic (N, E_g charge), Kekulé (K, A_{1K} charge), spontaneous current, or magnetoelectric (ME2, E_u charge), layer-polarized (LP, A_{2u} charge), Kekulé current (KC, A_{2K} charge), staggered spin current (SSC, A_{1u} spin), antiferromagnetic (AF, A_{2u} spin), quantum spin Hall (QSH, A_{2g} spin), s_{++} superconductor (s_{++} SC, A_{1g} singlet), and s_{+-} superconductor (s_{+-} SC, A_{2u} singlet) states. In addition to this fixed plane, we also find four isolated fixed points, which are described in the text.

ray at $\eta + \pi$. Due to the fact that any two opposite points at infinity on the target plane are identical, we conclude that the target plane is homeomorphic to a projective plane $\mathbb{R}P^2$. In Fig. 9, some of the phases, such as QSH, have hyperbolic phase boundaries and appear to exist in two disconnected parts of the phase diagram. However, due to the fact that the opposite points in the target plane are identical, these may be regarded as single and simply connected regions.

The values of $\rho_j^{(r)} = g_j/g_r$ are readily obtained from Eqs. (68)–(70). Without loss of generality we now set $g_r = g_{E_g}$ in Eq. (26). We obtain

$$\mathcal{A}_{(E_g)} = -6 \frac{3 + 2x + 3x^2 + 4y + 4xy + 8y^2}{1 + x + 2y} \frac{m^*}{4\pi}. \quad (71)$$

We may obtain $\mathcal{B}_{i,(E_g)}$ from Eqs. (33) and (34). We can now determine the anomalous dimensions of the symmetry-breaking source terms defined in Eq. (32). Remarkably, we see that the anomalous dimensions are continuous functions of the two parameters x and y. For each point in the target plane, we determine the phases for which $\eta_i > 1$, i.e., the inequality

Eq. (39) holds. If more than one phase satisfies this inequality, then we list all such phases regardless of the value of η_i. As discussed before, whenever two or more susceptibilities diverge, we cannot decide within our RG framework if the system chooses only one of these phases or if there is a coexistence. The resulting list of phases is shown in Fig. 9. In addition to the phases we found earlier in Sec. III E, namely the nematic (N), layer antiferromagnetic (AF), quantum spin Hall (QSH), layer-polarized (LP), Kekulé current (KC), and s_{++} superconducting (s_{++} SC) states, a few other phases are predicted as possible outcomes of the RG flow if it ends on the target plane. These are

(a) Magnetoelectric phase (ME2): the order parameter for this phase transforms according to the E_u charge representation. In this phase, currents forming a bow-tie pattern within a plaquette appear. Like the nematic phase, this phase is gapless, but it reconstructs the low-lying spectrum by lifting two of the four Dirac cones.

(b) Kekulé state (K): in this phase, a supercell made of three unit cells is formed, much like the Kekulé current phase.

The difference is that, in this phase, there are no currents. Instead, there is a modification of the hopping integrals such that the hoppings in one unit cell are unchanged, while, in the two other unit cells, the hoppings on alternating bonds are changed.[45] The phase is gapped.

(c) Staggered spin current state (SSC): this phase is characterized by circulating spin currents in each plaquette flowing in opposite directions in each layer. This phase is not gapped, corresponds to a compensated semimetal, and the order parameter belongs to the A_{1u} spin representation.

(d) s_{+-} superconducting state (s_{+-} SC): since a particle-particle susceptibility diverges in this case, a superconducting gap opens on both layers. The gaps are, however, not independent; they have opposite signs. The order parameter of this phase is a (charge 2) A_{2u} spin singlet.

Strictly speaking, when either x or y becomes infinite or they satisfy $1 + x + 2y = 0$, we are not allowed to divide by g_{E_g} as this coupling is not divergent. It shows up in Eq. (71) as a divergent $\mathcal{A}_{(E_g)}$. Instead, these cases are explored by dividing by some other coupling. We follow the same procedure as described above in the case where we divided by g_{E_g}. Interestingly, since both $\mathcal{A}_{(E_g)}$ and $\mathcal{B}_{i,(E_g)}$ diverge in the same way, the η_i's are independent of the choice of the coupling that we divide by.

In addition to the target plane, we also find the following four isolated stable fixed points.

R_1:

$$\lim_{\ell \to \infty} \frac{g_{A_{1g}}}{g_{E_g}}\bigg|_{t=t_c} = 3,$$
$$\lim_{\ell \to \infty} \frac{g_j}{g_{E_g}}\bigg|_{t=t_c} = 1 \quad \forall \ j \neq A_{1g}, \tag{72}$$

with $g_{E_g}(\ell \to \infty) > 0$. In this case, only the ferromagnetic (A_{1g} spin) susceptibility diverges.

R_2:

$$\lim_{\ell \to \infty} \frac{g_j}{g_{A_{2g}}}\bigg|_{t=t_c} = 0 \quad \forall \ j \neq A_{2g}, \tag{73}$$

and $g_{A_{2g}}(\ell \to \infty) < 0$. The only divergent susceptibility in this case is toward the anomalous quantum Hall state[43] (A_{2g} charge). Here, charge currents circulate in each layer,[37] and in the same direction in both layers.

R_3:

$$\lim_{\ell \to \infty} \frac{g_j}{g_{A_{1u}}}\bigg|_{t=t_c} = 0 \quad \forall \ j \neq A_{1u}, \tag{74}$$

and $g_{A_{1u}}(\ell \to \infty) < 0$. This yields a loop current order,[44] or "orbital antiferromagnet" (A_{1u} charge). Like the above phase, there are charge currents circulating in each layer, but in opposite directions. Note that the order parameter, $\tau_3 1$, can be thought of as a chemical potential shift with opposite signs in each valley. Therefore, at weak coupling, this phase corresponds to a compensated semimetal with electron and hole pockets.

R_4:

$$\lim_{\ell \to \infty} \frac{g_j}{g_{A_{1g}}}\bigg|_{t=t_c} = 0 \quad \forall \ j \neq A_{1g}, \tag{75}$$

with $g_{A_{1g}}(\ell \to \infty) < 0$. Although we would intuitively expect this fixed point to favor a superconducting state, we find no particle-particle susceptibilites diverging. Only the A_{1g} charge susceptibility, or equivalently the electronic compressibility, diverges. Therefore we conclude that the system enters a phase segregated state.

We can now make a connection between the results obtained in previous sections and the analytic results obtained here. For the set of initial couplings and parameters analyzed in Secs. III D–III F, the flow at t_c always converges to the target plane, and never to any of the isolated points R_j. In the case of forward scattering only at $\ell = 0$, and in the absence of trigonal warping, none of the couplings from the u and **K** representations are generated. The flow always ends at the point, $(x, y) = (0, 0)$, in the target plane, which corresponds to a pure nematic state. With trigonal warping included, u representation couplings are generated, even when we start with forward scattering only. However, we still do not generate any of the **K** representation couplings. This means that the end point of the flow at t_c is restricted to the $y = 0$ line in the target plane. Decreasing the initial coupling strength $g_{A_{1g}}$, while holding the bare v_3 fixed, causes t_c to decrease. At the same time, x increases. We always find that $x < 1$. As seen from Fig. 9, these points correspond to a pure nematic order. However, as t_c is lowered, the point in the target plane moves closer to $x = 1$, which is the intersection of the AF and QSH regions in the target plane. Upon reaching $t_c = 0$ exactly, we find that the nematic order parameter is absent while the AF and QSH susceptibilities become divergent. This is illustrated in Fig. 2(b). Note that there is no point at which the only two diverging susceptibilities are AF and QSH, either in the target plane or as one of the four isolated points. This is because the asymptotic behavior of the Φ functions is different at $t = 0$ and our analysis, in which we assumed that $t_c > 0$, does not apply there.

When the RG flow begins with a finite backscattering, i.e., $g_{E_\mathbf{K}} \neq 0$, all nine couplings are generated. We find that our numerical results correspond to points in the target plane where $y \neq 0$. With the physical constraints we impose on the initial couplings, $|g_{A_{2u}}| \leqslant g_{A_{1g}}$, $|g_{E_\mathbf{K}}| \leqslant g_{A_{1g}}/2$ and $g_{A_{1g}}$ positive, only the central region of the target plane is approached. With these constraints, we do not find any set of initial couplings for which K, SSC, or ME2 phases appear.

In the previous sections, the flows never reach any of the isolated points R_j. However, one can expect that the flow will tend to one of these points if one starts with bare couplings sufficiently close to the associated ray and with a large initial value of ℓ. To confirm this, we analyzed the flow equations with no trigonal warping and $g_{A_{1g}}(\ell = 0) < 0$. For sufficiently large initial values of the interaction $\frac{m^*}{4\pi} g_{A_{1g}}(\ell = 0) < \frac{m^*}{4\pi} g^c_{A_{1g}} \approx -0.13$, the flow takes the couplings towards the R_4 fixed ray. As stated before, this represents a compressibility instability. However, when $g_{A_{1g}}(\ell = 0) > g^c_{A_{1g}}$ the couplings diverge toward the nematic fixed ratio, i.e., our flows end up on the target plane.

The symmetry properties of the Hubbard limit have consequences for the asymptotic behavior of the RG flows studied in this section. When all three couplings, δg_i, Eqs. (57)–(59) are absent at the bare level, we have shown that they remain zero throughout the entire flow. As argued above, the ratios of

couplings at t_c must lie either on the target plane or at one of the four isolated points R_j. In the target plane, the condition, $\delta g_i = 0$, is satisfied only when $x = -2y$. This defines a line of fixed points (strictly speaking a circle, since two points at infinity are equivalent). As shown in Sec. III F, because $\delta g_i = 0$, the susceptibilities towards the layer-polarized and s_{++} superconducting states are identical. Therefore this holds along the entire line $x = -2y$. For the repulsive Hubbard model, a wide range of initial conditions, $10^{-8} < t_c < 1$, maps onto the segment of this fixed line that lies within the AF-only region. These results were also used in studying the attractive Hubbard model due to the $U \to -U$ correspondence presented in Sec. III F. The only difference is that both x and y change their sign under this mapping. The resulting fixed points are therefore situated in the region where the layer-polarized and s_{++} superconducting orders overlap.

In addition to the fixed line that is part of the target plane, the condition that all three δg_i's are zero is satisfied at the isolated fixed point R_1. However, we never find a flow toward that point for any set of bare couplings studied here.

IV. EFFECT OF A PERPENDICULAR ELECTRIC FIELD ON THE PHASE BOUNDARIES

We now consider the effect that applying a perpendicular electric field has on the phase boundaries of our system. This field creates an energy difference between the two layers of the sample, thus introducing a new term into the Hamiltonian,

$$\mathcal{H}_{E_\perp} = V_\perp \sum_{|\mathbf{k}| < \Lambda} \sum_{\sigma = \uparrow, \downarrow} \psi_{\mathbf{k}\sigma}^\dagger 1 \sigma_3 \psi_{\mathbf{k}\sigma}. \quad (76)$$

We state the effects that this has on the Green's function and on the associated identities that we use in Appendix B, and simply quote the main results here. The RG flow equations for the coupling constants become

$$\frac{dg_i}{d\ell} = \sum_{j,k} g_j g_k \sum_{a=1}^{6} A_{ijk}^{(a)} \Phi_a[v_3(\ell), v(\ell), t(\ell)], \quad (77)$$

where, in addition to the dimensionless parameters for the Φ functions that were defined before, we have one new parameter,

$$v(\ell) = \frac{V_\perp(\ell)}{\Lambda^2 / 2m^*}. \quad (78)$$

The Φ functions are given by Eqs. (B3)–(B15).

In addition, the energy difference $V_\perp$ has a nontrivial behavior under rescaling; it obeys the flow equation

$$\frac{dv}{d\ell} = 2v \left[1 + F(v_3, v, t) \sum_i b_i g_i \right], \quad (79)$$

where the coefficients b_i are given in Appendix C, and the function F is given by Eq. (B17).

We studied the behavior of the critical temperature as a function of v in a case where we know that the system enters the nematic phase when $v = 0$, namely, when all coupling constants are zero except for $g_{A_{1g}} > 0$. We assume that the energy scale $\frac{\Lambda^2}{2m^*} = 200$ meV, and that the critical temperature at zero field is $T_c = 2$ meV, i.e., $t_c = 0.01$. To determine t_c for a given initial $g_{A_{1g}}$, we start with a high value of t and integrate
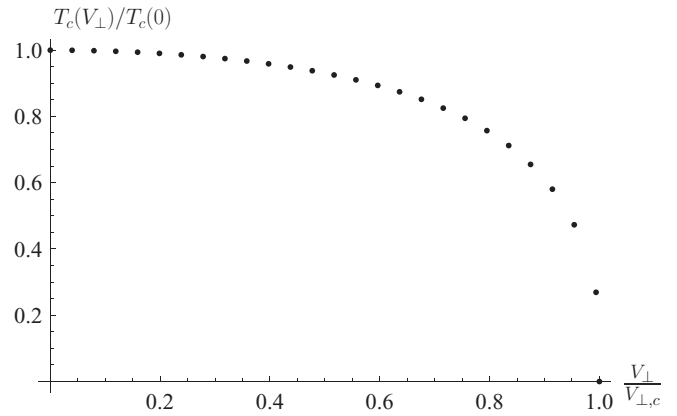

FIG. 10. Plot of the critical temperature T_c as a function of the layer energy difference $V_\perp$, under such conditions that $T_c(0) = 0.01\Lambda^2 / 2m^*$. The critical temperature becomes zero when $V_\perp = V_{\perp,c} = 4.93 \times 10^{-3} \Lambda^2 / 2m^*$, which corresponds to an applied electric field of ~ 16 mV/nm.

our RG flow equations numerically up to a large value of ℓ, say 10. If we do not encounter any divergences in the flows, we lower t and integrate again. We continue until we find the highest temperature at which we encounter a divergence. Under the stated conditions, the behavior of t_c as a function of v is as shown in Fig. 10.

We find that, at $v = 4.93 \times 10^{-3}$, t_c becomes zero. Converting this into an electric field using the stated energy scale and the formula relating the applied electric field to the size of the gap in the spectrum, $\Delta = \frac{dE}{k}$, where d is the distance between the two graphene layers and $k \approx 3$ is a factor accounting for imperfect screening,[4,5] we find that the electric field required to drive t_c to zero is ~ 16 mV/nm.

We have also determined which phase the system enters at all points on the curve in Fig. 10 at which $T_c \neq 0$. We did this by deriving the RG flow equations for the source terms and the formula for the free energy per unit area using the same procedures as before, but with properly modified Green's functions, whose forms are given in Appendix B. We then numerically integrate the RG flow equations, and, from these solutions, determine the susceptibilities to the phases corresponding to each source term just above the critical temperature; the phase with the highest susceptibility is considered to be the phase that is present. Using this procedure, we determined that, for all $V_\perp < V_{\perp,c}$, the system enters the nematic phase.

V. DISCUSSION

The key result of this work is the identification of the conditions on the electron-electron interactions under which various electronic ordering tendencies, if any, dominate in half-filled bilayer graphene. Our results for the ordered states are summarized in Figs. 5 and 9. Aside from our use of one-loop RG, no further approximations are made. Therefore our results can be stated rigorously at the level of mathematical theorems. While a large number of phases is, in principle, possible in the entire nine-dimensional space of couplings, as one can see from Fig. 9, our assertion is that the electronic nematic appears to be the unique dominant instability when forward scattering

dominates. Similarly, the layer antiferromagnet appears upon inclusion of sufficiently strong back and layer imbalance scattering.

A similar approach in one spatial dimension[22] results in divergences in the scattering amplitudes at finite temperature, naively suggesting a finite temperature phase transition, which we know cannot happen. Nevertheless, among many possibilities, the method does identify the correct channels for which long, but finite, correlation lengths develop. For example, the low-energy effective field theory for the course-grained half-filled Hubbard model does correctly determine that the dominant correlations appear in either the pairing (attractive U) or AF (repulsive U) channel.[54] Away from any special filling, a metallic state is also correctly predicted.[21]

We view our RG results for the half-filled Hubbard model similarly. While the method correctly determines the dominant ordering tendency, there can be no finite temperature phase transition in 2D to either the AF state or the SC/LP state. A continuous spin SU(2) symmetry in the former case, or a continuous pseudospin symmetry in the latter case, would have to be broken at finite temperature, which we know cannot happen. Therefore, if the RG procedure had been performed exactly, none of these susceptibilities would have diverged as long as the temperature was finite. Interestingly, in this regard, the nematic state is different. This is because, when trigonal warping is included, as it is in our model, the broken rotational symmetry is *discrete* and thus it is possible to have a finite-temperature transition into this phase in 2D. As argued previously,[11] this transition is continuous and belongs to the 3-state Potts model universality class.[49] Nevertheless, the *non-mean-field* exponents determined approximately from our fermionic model at one loop should not be expected to be accurate. It would be very interesting to see whether going to

higher order either improves the accuracy of the exponents in the case of the nematic state or eliminates the finite-temperature phase transition altogether for the case of $O(3)$ order parameters. The effects of (weak) disorder have not been addressed here either. These considerations may be important in fully understanding the current experimental results.[4–10]

Even if the RG method used here is not without its limitations, it is unbiased and capable of systematically treating the leading instabilities in both particle-hole and pairing channels. In fact, for a large range of temperatures above the transition temperature, the couplings saturate to small finite values as all modes are eliminated, giving full justification to our method. In the special case in which our continuum field theory corresponds to the weak-coupling honeycomb bilayer Hubbard model, we recover some of its nontrivial, exactly known, properties. This gives further support for the validity of our results.

APPENDIX A: ASYMPTOTIC BEHAVIOR OF THE Φ FUNCTIONS

The finite-temperature Green's function that is used to calculate the RG flows for infinitesimal symmetry breaking source terms is

$$G_{\mathbf{k}}(i\omega_n) = \left[-i\omega_n 1_8 + \frac{1}{2m^*}\left(k_x^2 - k_y^2\right)1\sigma_1 1 + v_3 k_x \tau_3 \sigma_1 1 + \frac{1}{m^*}k_x k_y \tau_3 \sigma_2 1 - v_3 k_y 1 \sigma_2 1 \right]^{-1} \tag{A1}$$

$$= \frac{1}{2}\sum_{s=\pm}(1 + s\tau_3)\frac{i\omega_n 1 + \left(\frac{1}{2m^*}k^2\cos 2\theta_{\mathbf{k}} + sv_3 k\cos\theta_{\mathbf{k}}\right)\sigma_1 + \left(s\frac{1}{2m^*}k^2\sin 2\theta_{\mathbf{k}} - v_3 k\sin\theta_{\mathbf{k}}\right)\sigma_2}{\omega_n^2 + \frac{1}{4m^{*2}}k^4 + v_3^2 k^2 + s\frac{1}{m^*}v_3 k^3\cos 3\theta_{\mathbf{k}}}1. \tag{A2}$$

Throughout the Appendix, we will use the notation, $\tau_i\sigma_j s_k$, for the (8×8) matrices that appear in our expressions; the Pauli matrices operate in valley, layer, and spin space, respectively. We find the following identity useful when calculating the flow equations:

$$\int_{\Lambda(1-d\ell)}^{\Lambda}\frac{dk k}{2\pi}\frac{1}{\beta}\sum_{n=-\infty}^{\infty}\int_{-\pi}^{\pi}\frac{d\theta_{\mathbf{k}}}{2\pi}G_{\mathbf{k}}(i\omega_n)\otimes G_{\pm\mathbf{k}}(\pm i\omega_n)$$

$$= d\ell\frac{m^*}{8\pi}\left\{\mp 1_8\otimes 1_8\left[\Phi_1(v_3,t)+\Phi_2(v_3,t)\right]+\frac{1}{2}\left(1\sigma_1 1\otimes 1\sigma_1 1 + \tau_3\sigma_2 1\otimes\tau_3\sigma_2 1\right)\left[\Phi_3(v_3,t)+\Phi_4(v_3,t)\right]\right\}$$

$$+ d\ell\frac{m^*}{8\pi}\left\{-\tau_3 1_4\otimes\tau_3 1_4\left[\Phi_1(v_3,t)-\Phi_2(v_3,t)\right]\pm\frac{1}{2}\left(\tau_3\sigma_1 1\otimes\tau_3\sigma_1 1 + 1\sigma_2 1\otimes 1\sigma_2 1\right)\left[\Phi_4(v_3,t)-\Phi_3(v_3,t)\right]\right\}. \tag{A3}$$

The Φ functions are defined as

$$\Phi_1(v_3,t) = \frac{1}{2\pi}\frac{1}{t}\int_{-1}^{1}\frac{dx}{\sqrt{1-x^2}}\Upsilon_1(x,v_3,t), \tag{A4}$$

$$\Phi_2(v_3,t) = \frac{1}{\pi}\frac{1}{v_3}\int_{0}^{1}\frac{dx}{\sqrt{1-x^2}}\frac{1}{x}\Upsilon_2(x,v_3,t), \tag{A5}$$

$$\Phi_3(v_3,t) = \frac{1}{\pi}\frac{1-v_3^2}{v_3}\int_0^1 \frac{dx}{\sqrt{1-x^2}}\frac{1}{x}\Upsilon_3(x,v_3,t), \quad (A6)$$

$$\Phi_4(v_3,t) = \frac{1}{2\pi}\frac{1}{t}\int_{-1}^1 \frac{dx}{\sqrt{1-x^2}}\Upsilon_4(x,v_3,t), \quad (A7)$$

where

$$\Upsilon_1(x,v_3,t) = \frac{1}{\cosh^2\left(\frac{Q_+}{2t}\right)} + \frac{2t}{Q_+}\tanh\left(\frac{Q_+}{2t}\right), \quad (A8)$$

$$\Upsilon_2(x,v_3,t) = \sum_{\lambda=\pm}\lambda Q_\lambda \tanh\left(\frac{Q_\lambda}{2t}\right), \quad (A9)$$

$$\Upsilon_3(x,v_3,t) = -\sum_{\lambda=\pm}\frac{\lambda}{Q_\lambda}\tanh\left(\frac{Q_\lambda}{2t}\right), \quad (A10)$$

$$\Upsilon_4(x,v_3,t) = \frac{-1}{\cosh^2\left(\frac{Q_+}{2t}\right)} + \frac{2t}{Q_+}\tanh\left(\frac{Q_+}{2t}\right), \quad (A11)$$

and

$$Q_\pm = \sqrt{1+v_3^2 \pm 2xv_3}. \quad (A12)$$

In the limit of $v_3 = 0$, we have

$$\Phi_1(0,t) = \Phi_2(0,t) = \tanh\frac{1}{2t} + \frac{1}{2t}\frac{1}{\cosh^2\frac{1}{2t}}, \quad (A13)$$

$$\Phi_3(0,t) = \Phi_4(0,t) = \tanh\frac{1}{2t} - \frac{1}{2t}\frac{1}{\cosh^2\frac{1}{2t}}. \quad (A14)$$

In the limit of $T = 0$, we have

$$\Phi_1(v_3,0) = \Phi_4(v_3,0) = \frac{2}{\pi}\frac{1}{1+v_3}K\left[\frac{4v_3}{(1+v_3)^2}\right], \quad (A15)$$

$$\Phi_2(v_3,0) = \frac{2}{\pi}\frac{1}{v_3}\frac{(1-v_3)^2}{1+v_3}\left\{\Pi\left[\frac{2v_3}{1+v_3^2},\frac{4v_3}{(1+v_3)^2}\right]\right.$$
$$\left. - K\left[\frac{4v_3}{(1+v_3)^2}\right]\right\}, \quad (A16)$$

$$\Phi_3(v_3,0) = \frac{2}{\pi}\frac{1-v_3}{v_3}\left\{K\left[\frac{4v_3}{(1+v_3)^2}\right]\right.$$
$$\left. - \frac{(1-v_3)^2}{1+v_3^2}\Pi\left[\frac{2v_3}{1+v_3^2},\frac{4v_3}{(1+v_3)^2}\right]\right\}. \quad (A17)$$

Here, the complete elliptic integrals of the first, $K(x)$, and the third, $\Pi(x,y)$, kind are defined as

$$K(x) = \int_0^{\frac{\pi}{2}} \frac{d\phi}{\sqrt{1-x\sin^2\phi}}, \quad (A18)$$

$$\Pi(x,y) = \int_0^{\frac{\pi}{2}} \frac{d\phi}{(1-x\sin^2\phi)\sqrt{1-y\sin^2\phi}}. \quad (A19)$$

Physically, the logarithmic singularity associated with $K(x)$ has its origin in the logarithmic divergence of the density of states at the van Hove point, where the lines of constant energy near each **K** point change from single to four closed contours. These log singularities appear only at $t = 0$, for $t > 0$ they are smeared out. Because the divergences are integrable, they aren't the cause of divergence of $g_i's$ in Eq. (19). Instead, the coupling constants receive a "boost" at ℓ, where $v_3(\ell) = 1$.

APPENDIX B: GREEN'S FUNCTIONS IN THE PRESENCE OF AN APPLIED PERPENDICULAR ELECTRIC FIELD

In the presence of an applied electric field, the Green's function becomes

$$G_{\mathbf{k}}(i\omega_n) = \left(-i\omega_n 1_8 + d_{\mathbf{k}}^x 1\sigma_1 1 + v_3 k_x \tau_3\sigma_1 1 + d_{\mathbf{k}}^y \tau_3\sigma_2 1 - v_3 k_y 1\sigma_2 1 + V_\perp 1\sigma_3 1\right)^{-1}$$

$$= \frac{1}{2}\sum_{s=\pm}(1+s\tau_3)\frac{i\omega_n 1 + \left(\frac{1}{2m^*}k^2\cos 2\theta + sv_3 k\cos\theta\right)\sigma_1 + \left(s\frac{1}{2m^*}k^2\sin 2\theta - v_3 k\sin\theta\right)\sigma_2 + V_\perp 1\sigma_3}{\omega_n^2 + \frac{1}{4m^{*2}}k^4 + v_3^2 k^2 + s\frac{1}{m^*}v_3 k^3\cos 3\theta + V_\perp^2}1. \quad (B1)$$

The generalization of Eq. (A3) for this case is

$$\int_{\Lambda(1-d\ell)}^{\Lambda}\frac{k\,dk}{2\pi}\frac{1}{\beta}\sum_{n=-\infty}^{\infty}\int_0^{2\pi}\frac{d\theta_{\mathbf{k}}}{2\pi}G_{\mathbf{k}}(i\omega_n)\otimes G_{\pm\mathbf{k}}(\pm i\omega_n)$$

$$= \frac{m^*}{8\pi}d\ell\left[(\mp 1_8\otimes 1_8 - \tau_3 1_4\otimes\tau_3 1_4)\Phi_1(v_3,v,t) + (\mp 1_8\otimes 1_8 + \tau_3 1_4\otimes\tau_3 1_4)\Phi_2(v_3,v,t)\right.$$

$$+ \frac{1}{2}(1\sigma_1 1\otimes 1\sigma_1 1 \mp \tau_3\sigma_1 1\otimes\tau_3\sigma_1 1 \mp 1\sigma_2 1\otimes 1\sigma_2 1 + \tau_3\sigma_2 1\otimes\tau_3\sigma_2 1)\Phi_3(v_3,v,t)$$

$$+ \frac{1}{2}(1\sigma_1 1\otimes 1\sigma_1 1 \pm \tau_3\sigma_1 1\otimes\tau_3\sigma_1 1 \pm 1\sigma_2 1\otimes 1\sigma_2 1 + \tau_3\sigma_2 1\otimes\tau_3\sigma_2 1)\Phi_4(v_3,v,t)$$

$$\left. + (1\sigma_3 1\otimes 1\sigma_3 1 + \tau_3\sigma_3 1\otimes\tau_3\sigma_3 1)\Phi_5(v_3,v,t) + (1\sigma_3 1\otimes 1\sigma_3 1 - \tau_3\sigma_3 1\otimes\tau_3\sigma_3 1)\Phi_6(v_3,v,t)\right], \quad (B2)$$

where the Φ functions are

$$\Phi_1(v_3,v,t) = \frac{1}{2\pi}\frac{1}{t}\int_{-1}^1 \frac{dx}{\sqrt{1-x^2}}\Upsilon_1(x,v_3,v,t), \quad (B3)$$

$$\Phi_2(v_3,v,t) = \frac{1}{\pi} \frac{1}{v_3} \int_0^1 \frac{dx}{\sqrt{1-x^2}} \frac{1}{x} \Upsilon_2(x,v_3,v,t), \quad \text{(B4)}$$

$$\Phi_3(v_3,v,t) = \frac{1}{\pi} \frac{1-v_3^2}{v_3} \int_0^1 \frac{dx}{\sqrt{1-x^2}} \frac{1}{x} \Upsilon_3(x,v_3,v,t), \quad \text{(B5)}$$

$$\Phi_4(v_3,v,t) = \frac{1}{2\pi} \frac{1}{t} \int_{-1}^1 \frac{dx}{\sqrt{1-x^2}} \Upsilon_4(x,v_3,v,t), \quad \text{(B6)}$$

$$\Phi_5(v_3,v,t) = \frac{1}{2\pi} \frac{v^2}{t} \int_{-1}^1 \frac{dx}{\sqrt{1-x^2}} \Upsilon_5(x,v_3,v,t), \quad \text{(B7)}$$

$$\Phi_6(v_3,v,t) = \frac{v^2}{1-v_3^2} \Phi_3(v_3,v,t). \quad \text{(B8)}$$

The Υ functions are

$$\Upsilon_1(x,v_3,v,t) = \frac{2t}{Q_+} \tanh\left(\frac{Q_+}{2t}\right) + \frac{1}{\cosh^2\left(\frac{Q_+}{2t}\right)}, \quad \text{(B9)}$$

$$\Upsilon_2(x,v_3,v,t) = \sum_{\lambda=\pm} \lambda Q_\lambda \tanh\left(\frac{Q_\lambda}{2t}\right), \quad \text{(B10)}$$

$$\Upsilon_3(x,v_3,v,t) = -\sum_{\lambda=\pm} \frac{\lambda}{Q_\lambda} \tanh\left(\frac{Q_\lambda}{2t}\right), \quad \text{(B11)}$$

$$\Upsilon_4(x,v_3,v,t) = \left(\frac{Q_+^{(0)}}{Q_+}\right)^2 \left[\frac{2t}{Q_+} \tanh\left(\frac{Q_+}{2t}\right) - \frac{1}{\cosh^2\left(\frac{Q_+}{2t}\right)}\right], \quad \text{(B12)}$$

$$\Upsilon_5(x,v_3,v,t) = \frac{1}{(Q_+^{(0)})^2} \Upsilon_4(x,v_3,v,t), \quad \text{(B13)}$$

where

$$Q_\pm = \sqrt{1+v_3^2+v^2 \pm 2xv_3}, \quad \text{(B14)}$$

$$Q_\pm^{(0)} = \sqrt{1+v_3^2 \pm 2xv_3}. \quad \text{(B15)}$$

One other identity that we will find useful is

$$\int_{\Lambda(1-d\ell)}^{\Lambda} \frac{k\,dk}{2\pi} \frac{1}{\beta} \sum_{n=-\infty}^{\infty} \int_0^{2\pi} \frac{d\theta_{\mathbf{k}}}{2\pi} G_{\mathbf{k}}(i\omega_n)$$
$$= \frac{m^* V_\perp}{2\pi} 1\sigma_3 1 F(v_3,v,t)\,d\ell, \quad \text{(B16)}$$

where $F(v_3,v,t)$ is

$$F(v_3,v,t) = \frac{1}{\pi} \int_{-1}^1 \frac{dx}{\sqrt{1-x^2}} \frac{1}{Q_+} \tanh\left(\frac{Q_+}{2t}\right). \quad \text{(B17)}$$

In arriving at this result, we will, in the intermediate steps, also find a term proportional to $\tau_3\sigma_3 1$. However, we can use the periodicity of the integrand to show that this term will be zero at the end. We can also see that this must happen due to the symmetries of our system. Imagine that we tried calculating the expectation value of an observable, which would be represented by a matrix $\tau_i\sigma_j s_k$. This expectation value will only be nonzero if the matrix is proportional to one of the matrices appearing in the above identity, since said expectation value involves a trace of the product of the Green's function with the associated matrix. If a term proportional to $\tau_3\sigma_3 1$ were present, then this means that we can have a finite expectation value of the associated observable, which would,

in this case, correspond to the gap opened by an anomalous quantum Hall order parameter. This order parameter breaks time reversal symmetry. However, we should not be able to develop a finite expectation value of this observable because our Hamiltonian is time reversal invariant.

APPENDIX C: DETERMINATION OF RG FLOW EQUATIONS

We now show how to derive the flow equations for the four-fermion coupling constants g and the source term constants Δ. We start by performing a cumulant expansion of the partition function to second order in the "perturbation" $S_{\text{int}} + \Delta S$:

$$Z \approx \exp\left[-\langle S_{\text{int}} + \Delta S \rangle_0 + \frac{1}{2}\langle (S_{\text{int}} + \Delta S)^2 \rangle_{0,C}\right], \quad \text{(C1)}$$

where, in the subscripts on the averages $\langle\cdots\rangle$, "0" means to average with respect to the bare action S_0, and "C" means that the average is "connected," that is, it can be represented with connected Feynman diagrams. We now integrate out modes in thin shells; by doing so, we generate terms that renormalize different constants in our theory. We will first discuss the terms that renormalize the four-fermion coupling constants, since the general procedure is the same. There are five different types of terms that appear; these are represented by the diagrams shown in Fig. 11.

The first diagram gives the following correction:

$$\delta S_1 = \frac{1}{2} \sum_{S,U} g_S g_U \int_{1,2,3,4} \left\{\iint_{\mathbf{k}_>,\omega} \text{Tr}[S1G_{\mathbf{k}}(i\omega)U1G_{\mathbf{k}}(i\omega)]\right\}$$
$$\times \sum_{\sigma,\sigma'} \psi_\sigma^\dagger(1) S \psi_\sigma(2) \psi_{\sigma'}^\dagger(3) U \psi_{\sigma'}(4), \quad \text{(C2)}$$

where the numbers 1–4 are shorthand for the momentum and frequency dependencies of the Grassman fields, and $\int_{1,2,3,4}$ represents the integrals and sums over these variables along with the proper momentum- and frequency-conserving δ functions, and similarly for $\int_{\mathbf{k}_>,\omega}$. We may evaluate the integral and sum over $\mathbf{k}$ and ω, respectively, using Eq. (A3) in the absence of an external electric field or Eq. (B2) when said field is present. In both cases, this term is only nonzero if $S = U$, so that we generate a correction to g_S that is proportional to g_S^2. The nonzero contributions to the coefficients

$$A_{ijk}^{(a)} = A_{ijk}^{(a)}(1) + A_{ijk}^{(a)}(2+3) + A_{ijk}^{(a)}(4) + A_{ijk}^{(a)}(5) \quad \text{(C3)}$$

in Eq. (19) are

$$A_{iii}^{(1/2)}(1) = -\frac{1}{2}\left\{8 \pm \text{Tr}\left[\left(\Gamma_i^{(1)}\tau_3 1_4\right)^2\right]\right\}\frac{m^*}{4\pi}, \quad \text{(C4)}$$
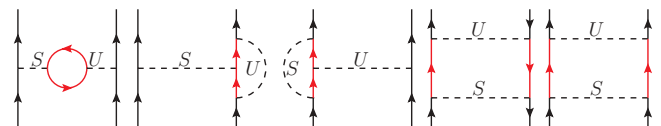

FIG. 11. (Color online) Diagrams representing contributions to the renormalization of the four-fermion coupling constants g_i. The dashed lines represent 8×8 matrices, the black lines represent slow modes, and the red lines represent fast modes.

$$A_{iii}^{(3/4)}(1) = \frac{1}{4}\left\{\text{Tr}\left[\left(\Gamma_i^{(1)}1\sigma_1 1\right)^2\right] \mp \text{Tr}\left[\left(\Gamma_i^{(1)}\tau_3\sigma_1 1\right)^2\right]\right.$$

$$\left.\mp \text{Tr}\left[\left(\Gamma_i^{(1)}1\sigma_2 1\right)^2\right] + \text{Tr}\left[\left(\Gamma_i^{(1)}\tau_3\sigma_2 1\right)^2\right]\right\}\frac{m^*}{4\pi}, \quad \text{(C5)}$$

$$A_{iii}^{(5/6)}(1) = \frac{1}{2}\left\{\text{Tr}\left[\left(\Gamma_i^{(1)}1\sigma_3 1\right)^2\right] \pm \text{Tr}\left[\left(\Gamma_i^{(1)}\tau_3\sigma_3 1\right)^2\right]\right\}\frac{m^*}{4\pi}. \quad \text{(C6)}$$

In these expressions, the top signs correspond to the first number in the superscript on the left-hand side, while the bottom corresponds to the second. The $A_{ijk}^{(5/6)}$ coefficients only enter into our analysis when a finite electric field is present. The 8×8 matrices $\Gamma_i^{(m)}$ are defined as follows:

$$\Gamma_1^{(1)} = 1_8, \quad \text{(C7)}$$

$$\Gamma_2^{(1)} = \tau_3\sigma_3 1, \quad \text{(C8)}$$

$$\Gamma_3^{(1)} = 1\sigma_1 1, \quad \Gamma_3^{(2)} = \tau_3\sigma_2 1, \quad \text{(C9)}$$

$$\Gamma_4^{(1)} = \tau_3 1_4, \quad \text{(C10)}$$

$$\Gamma_5^{(1)} = 1\sigma_3 1, \quad \text{(C11)}$$

$$\Gamma_6^{(1)} = \tau_3\sigma_1 1, \quad \Gamma_6^{(2)} = -1\sigma_2 1, \quad \text{(C12)}$$

$$\Gamma_7^{(1)} = \tau_1\sigma_1 1, \quad \Gamma_7^{(2)} = \tau_2\sigma_1 1, \quad \text{(C13)}$$

$$\Gamma_8^{(1)} = \tau_1\sigma_2 1, \quad \Gamma_8^{(2)} = \tau_2\sigma_2 1, \quad \text{(C14)}$$

$$\Gamma_9^{(1)} = \tau_1 1_4, \quad \Gamma_9^{(2)} = -\tau_2\sigma_3 1,$$
$$\Gamma_9^{(3)} = -\tau_2 1_4, \quad \Gamma_9^{(4)} = -\tau_1\sigma_3 1. \quad \text{(C15)}$$

The superscripts (m) refer to the multiplicity of a given representation. Here, and throughout this appendix, $A_{ijk}^{(a)}(n)$ represents the contribution to $A_{ijk}^{(a)}$ from the nth diagram in Fig. 11.

The second and third diagrams together give the following correction:

$$\delta S_{2+3} = -\sum_{S,U} g_S g_U \int_{1,2,3,4} \psi_\sigma^\dagger(1) S \psi_\sigma(2) \psi^\dagger(3)$$

$$\times \left[\int_{\mathbf{k}_>,\omega} U1 G_{\mathbf{k}}(i\omega) S1 G_{\mathbf{k}}(i\omega) U1\right] \psi(4). \quad \text{(C16)}$$

Note that the first two ψ fields carry an explicit spin index. The second two do not; for notational simplicity, these two are extended to be eight-component spinors in valley, layer, and spin space. In both cases that we consider, the second matrix $U1 G_{\mathbf{k}}(i\omega) S1 G_{\mathbf{k}}(i\omega) U1$ appearing in this expression is proportional to $S1$. Therefore this term also represents a correction to g_S, but now it generates terms involving the products, $g_S g_U$. We may extract the contributions to the $A_{ijk}^{(a)}$ coefficients by noting that, since the second matrix is proportional to $S1$. Using $\text{Tr}(\Gamma_i^{(m)}\Gamma_j^{(n)}) = 8\delta_{ij}\delta_{mn}$, we find that the nonzero contributions to the $A_{ijk}^{(a)}$ coefficients are

$$A_{iij}^{(1/2)}(2+3) = \frac{1}{8}\sum_{m=1}^{m_j}\left\{\text{Tr}\left[\left(\Gamma_i^{(1)}\Gamma_j^{(m)}\right)^2\right] \pm \text{Tr}\left(\Gamma_i^{(1)}\Gamma_j^{(m)}\tau_3 1_4\Gamma_i^{(1)}\tau_3 1_4\Gamma_j^{(m)}\right)\right\}\frac{m^*}{4\pi}, \quad \text{(C17)}$$

$$A_{iij}^{(3/4)}(2+3) = -\frac{1}{16}\sum_{m=1}^{m_j}\left[\text{Tr}\left(\Gamma_i^{(1)}\Gamma_j^{(m)}1\sigma_1 1\Gamma_i^{(1)}1\sigma_1 1\Gamma_j^{(m)}\right) \mp \text{Tr}\left(\Gamma_i^{(1)}\Gamma_j^{(m)}\tau_3\sigma_1 1\Gamma_i^{(1)}\tau_3\sigma_1 1\Gamma_j^{(m)}\right)\right.$$

$$\left.\mp \text{Tr}\left(\Gamma_i^{(1)}\Gamma_j^{(m)}1\sigma_2 1\Gamma_i^{(1)}1\sigma_2 1\Gamma_j^{(m)}\right) + \text{Tr}\left(\Gamma_i^{(1)}\Gamma_j^{(m)}\tau_3\sigma_2 1\Gamma_i^{(1)}\tau_3\sigma_2 1\Gamma_j^{(m)}\right)\right]\frac{m^*}{4\pi}, \quad \text{(C18)}$$

$$A_{iij}^{(5/6)}(2+3) = -\frac{1}{8}\sum_{m=1}^{m_j}\left[\text{Tr}\left(\Gamma_i^{(1)}\Gamma_j^{(m)}1\sigma_3 1\Gamma_i^{(1)}1\sigma_3 1\Gamma_j^{(m)}\right) \pm \text{Tr}\left(\Gamma_i^{(1)}\Gamma_j^{(m)}\tau_3\sigma_3 1\Gamma_i^{(1)}\tau_3\sigma_3 1\Gamma_j^{(m)}\right)\right]\frac{m^*}{4\pi}. \quad \text{(C19)}$$

Here, the sum on m is taken over the multiplicity of the jth representation, and the "2 + 3" in the "arguments" means that the given contribution is the total contribution from the second and third diagrams.

Finally, the fourth and fifth diagrams give the following:

$$\delta S_4 = -\frac{1}{2}\sum_{S,U} g_S g_U \int_{1,2,3,4}\int_{\mathbf{k}_>,\omega}\psi^\dagger(1) S G_{\mathbf{k}}(i\omega) U \psi(2)\psi^\dagger(3) U G_{\mathbf{k}}(i\omega) S\psi(4), \quad \text{(C20)}$$

$$\delta S_5 = -\frac{1}{2}\sum_{S,U} g_S g_U \int_{1,2,3,4}\int_{\mathbf{k}_>,\omega}\psi^\dagger(1) S G_{\mathbf{k}}(i\omega) U \psi(2)\psi^\dagger(3) S G_{-\mathbf{k}}(-i\omega) U\psi(4). \quad \text{(C21)}$$

Both matrices occurring in each expression are proportional to each other, but will in general not be proportional to either S or U. These terms therefore represent corrections to a coupling g_V that are proportional to $g_S g_U$. Using the same observation as before, we can find the contributions to the $A_{ijk}^{(a)}$ coefficients. Denoting $V = \Gamma_k$, these are

$$A_{kij}^{(1/2)}(4) = \frac{1}{128}\sum_{m=1}^{m_i}\sum_{n=1}^{m_j}\left[\text{Tr}\left(\Gamma_k^{(1)}\Gamma_i^{(m)}\Gamma_j^{(n)}\right)\text{Tr}\left(\Gamma_k^{(1)}\Gamma_j^{(n)}\Gamma_i^{(m)}\right) \pm \text{Tr}\left(\Gamma_k^{(1)}\Gamma_i^{(m)}\tau_3 1_4\Gamma_j^{(n)}\right)\text{Tr}\left(\Gamma_k^{(1)}\Gamma_j^{(n)}\tau_3 1_4\Gamma_i^{(m)}\right)\right]\frac{m^*}{4\pi}, \quad \text{(C22)}$$
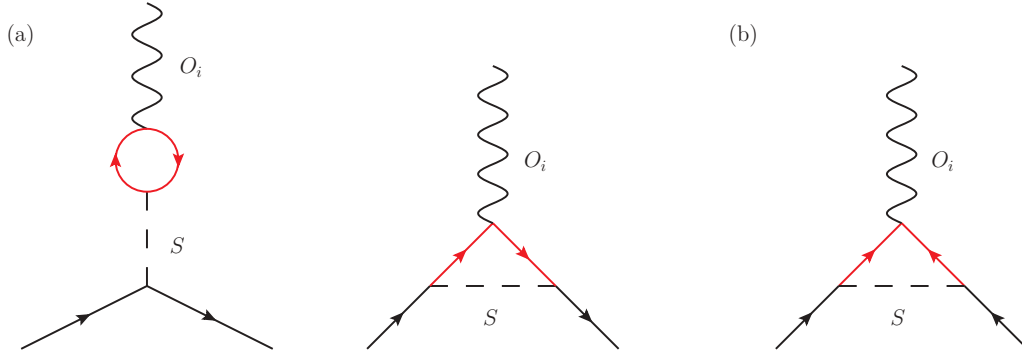
FIG. 12. (Color online) (a) Diagrams representing contributions to the renormalization of the particle-hole source terms. All lines are as in Fig. 11. In addition, the wavy lines represent the source terms. (b) Diagram representing contributions to the renormalization of the particle-particle source terms.

$$A_{kij}^{(3/4)}(4) = -\frac{1}{256}\sum_{m=1}^{m_i}\sum_{n=1}^{m_j}\Big[\text{Tr}\big(\Gamma_k^{(1)}\Gamma_i^{(m)}1\sigma_1 1\Gamma_j^{(n)}\big)\text{Tr}\big(\Gamma_k^{(1)}\Gamma_j^{(n)}1\sigma_1 1\Gamma_i^{(m)}\big) \mp \text{Tr}\big(\Gamma_k^{(1)}\Gamma_i^{(m)}\tau_3\sigma_1 1\Gamma_j^{(n)}\big)\text{Tr}\big(\Gamma_k^{(1)}\Gamma_j^{(n)}\tau_3\sigma_1 1\Gamma_i^{(m)}\big)$$

$$\mp \text{Tr}\big(\Gamma_k^{(1)}\Gamma_i^{(m)}1\sigma_2 1\Gamma_j^{(n)}\big)\text{Tr}\big(\Gamma_k^{(1)}\Gamma_j^{(n)}1\sigma_2 1\Gamma_i^{(m)}\big) + \text{Tr}\big(\Gamma_k^{(1)}\Gamma_i^{(m)}\tau_3\sigma_2 1\Gamma_j^{(n)}\big)\text{Tr}\big(\Gamma_k^{(1)}\Gamma_j^{(n)}\tau_3\sigma_2 1\Gamma_i^{(m)}\big)\Big]\frac{m^*}{4\pi}, \tag{C23}$$

$$A_{kij}^{(5/6)}(4) = \frac{-1}{128}\sum_{m=1}^{m_i}\sum_{n=1}^{m_j}\Big[\text{Tr}\big(\Gamma_k^{(1)}\Gamma_i^{(m)}1\sigma_3 1\Gamma_j^{(n)}\big)\text{Tr}\big(\Gamma_k^{(1)}\Gamma_j^{(n)}1\sigma_3 1\Gamma_i^{(m)}\big) \pm \text{Tr}\big(\Gamma_k^{(1)}\Gamma_i^{(m)}\tau_3\sigma_3 1\Gamma_j^{(n)}\big)\text{Tr}\big(\Gamma_k^{(1)}\Gamma_j^{(n)}\tau_3\sigma_3 1\Gamma_i^{(m)}\big)\Big]\frac{m^*}{4\pi}, \tag{C24}$$

and

$$A_{kij}^{(1/2)}(5) = -\frac{1}{128}\sum_{m=1}^{m_i}\sum_{n=1}^{m_j}\Big\{\big[\text{Tr}\big(\Gamma_k^{(1)}\Gamma_i^{(m)}\Gamma_j^{(n)}\big)\big]^2 \mp \big[\text{Tr}\big(\Gamma_k^{(1)}\Gamma_i^{(m)}\tau_3 1_4\Gamma_j^{(n)}\big)\big]^2\Big\}\frac{m^*}{4\pi}, \tag{C25}$$

$$A_{kij}^{(3/4)}(5) = -\frac{1}{256}\sum_{m=1}^{m_i}\sum_{n=1}^{m_j}\Big\{\big[\text{Tr}\big(\Gamma_k^{(1)}\Gamma_i^{(m)}1\sigma_1 1\Gamma_j^{(n)}\big)\big]^2 \pm \big[\text{Tr}\big(\Gamma_k^{(1)}\Gamma_i^{(m)}\tau_3\sigma_1 1\Gamma_j^{(n)}\big)\big]^2$$

$$\pm \big[\text{Tr}\big(\Gamma_k^{(1)}\Gamma_i^{(m)}1\sigma_2 1\Gamma_j^{(n)}\big)\big]^2 + \big[\text{Tr}\big(\Gamma_k^{(1)}\Gamma_i^{(m)}\tau_3\sigma_2 1\Gamma_j^{(n)}\big)\big]^2\Big\}\frac{m^*}{4\pi}, \tag{C26}$$

$$A_{kij}^{(5/6)}(5) = -\frac{1}{128}\sum_{m=1}^{m_i}\sum_{n=1}^{m_j}\Big\{\big[\text{Tr}\big(\Gamma_k^{(1)}\Gamma_i^{(m)}1\sigma_3 1\Gamma_j^{(n)}\big)\big]^2 \pm \big[\text{Tr}\big(\Gamma_k^{(1)}\Gamma_i^{(m)}\tau_3\sigma_3 1\Gamma_j^{(n)}\big)\big]^2\Big\}\frac{m^*}{4\pi}. \tag{C27}$$

We now turn our attention to the symmetry-breaking source terms. In this case, we have different procedures for the case without an applied electric field and the case with one. We will consider the former case first. The corrections to the particle-hole and particle-particle source terms are represented by the diagrams in Fig. 12.

The particle-hole source term corrections give us

$$\delta S_{\text{ph}} = \sum_i \sum_S \Delta_i^{\text{ph}} g_S \int_{\mathbf{k}'_<,\omega'}\int_{\mathbf{k}_>,\omega}\text{Tr}[G_{\mathbf{k}}(i\omega)O^{(i)}G_{\mathbf{k}}(i\omega)S1]\psi_{\mathbf{k}'}^\dagger(\omega')S1\psi_{\mathbf{k}'}(\omega')$$

$$- \sum_i \sum_S \Delta_i^{\text{ph}} g_S \int_{\mathbf{k}'_<,\omega'}\int_{\mathbf{k}_>,\omega}\psi_{\mathbf{k}'}^\dagger(\omega')S1 G_{\mathbf{k}}(i\omega)O^{(i)}G_{\mathbf{k}}(i\omega)S1\psi_{\mathbf{k}'}(\omega'). \tag{C28}$$

In the first term, the trace will only be nonzero if $S1 = O^{(i)}$, and, in the second term, the matrix appearing in the expression is proportional to $O^{(i)}$. Therefore we see that different source terms are not mixed to this order. Note that the first term is only nonzero if $O^{(i)}$ represents a charge order, and vanishes for spin orders. The contributions to the coefficients

$$B_{ij}^{(a)} = B_{ij}^{(a)}(1) + B_{ij}^{(a)}(2) \tag{C29}$$

in Eq. (28) are

$$B_{ij}^{(1/2)}(1) = -\frac{1}{2}\sum_{n=1}^{m_j}\big[\text{Tr}\big(O^{(i)}\Gamma_j^{(n)}\big) \pm \text{Tr}\big(\tau_3 1_4 O^{(i)}\tau_3 1_4\Gamma_j^{(n)}\big)\big]\frac{m^*}{4\pi}, \tag{C30}$$

$$B_{ij}^{(3/4)}(1) = \frac{1}{4} \sum_{n=1}^{m_j} \left[\text{Tr}\left(1\sigma_1 1 O^{(i)} 1\sigma_1 1\Gamma_j^{(n)}\right) \mp \text{Tr}\left(\tau_3\sigma_1 1 O^{(i)} \tau_3\sigma_1 1\Gamma_j^{(n)}\right) \mp \text{Tr}\left(1\sigma_2 1 O^{(i)} 1\sigma_2 1\Gamma_j^{(n)}\right) + \text{Tr}\left(\tau_3\sigma_2 1 O^{(i)} \tau_3\sigma_2 1\Gamma_j^{(n)}\right) \right] \frac{m^*}{4\pi},$$

(C31)

$$B_{ij}^{(1/2)}(2) = \frac{1}{16} \sum_{n=1}^{m_j} \left\{ \text{Tr}\left[\left(O^{(i)}\Gamma_j^{(n)}\right)^2\right] \pm \text{Tr}\left(O^{(i)}\Gamma_j^{(n)}\tau_3 1_4 O^{(i)}\tau_3 1_4 \Gamma_j^{(n)}\right) \right\} \frac{m^*}{4\pi},$$

(C32)

$$B_{ij}^{(3/4)}(2) = -\frac{1}{32} \sum_{n=1}^{m_j} \left[\text{Tr}\left(O^{(i)}\Gamma_j^{(n)} 1\sigma_1 1 O^{(i)} 1\sigma_1 1\Gamma_j^{(n)}\right) \mp \text{Tr}\left(O^{(i)}\Gamma_j^{(n)}\tau_3\sigma_1 1 O^{(i)}\tau_3\sigma_1 1\Gamma_j^{(n)}\right) \right.$$

$$\left. \mp \text{Tr}\left(O^{(i)}\Gamma_j^{(n)} 1\sigma_2 1 O^{(i)} 1\sigma_2 1\Gamma_j^{(n)}\right) + \text{Tr}\left(O^{(i)}\Gamma_j^{(n)}\tau_3\sigma_2 1 O^{(i)}\tau_3\sigma_2 1\Gamma_j^{(n)}\right) \right] \frac{m^*}{4\pi}.$$

(C33)

Here, the "arguments" have the same meaning as before, but with respect to Fig. 12.

The correction to the particle-particle source term is

$$\delta S_{\text{pp}} = -\frac{1}{2} \sum_{i=1}^{16} \sum_S \Delta_i^{\text{pp}} g_S \int_{\mathbf{k}'_<,\omega'} \int_{\mathbf{k}_>,\omega} \psi_{\mathbf{k}'}^\dagger(\omega') S 1 G_{\mathbf{k}}(i\omega) \tilde{O}^{(i)}$$

$$\times [G_{-\mathbf{k}}(-i\omega)]^T (S1)^T \psi_{-\mathbf{k}'}^*(-\omega') + \text{c.c.} \quad \text{(C34)}$$

For similar reasons as above, the product of five matrices appearing in this expression is proportional to $\tilde{O}^{(i)}$, and therefore different source terms are not mixed to this order. Also note that the 8×8 matrix $\tilde{O}^{(i)}$ must be completely antisymmetric. The values of the coefficients $\tilde{B}_{ij}^{(a)}$ in Eq. (29) are therefore

$$\tilde{B}_{ij}^{(1/2)} = -\frac{1}{16} \sum_{n=1}^{m_j} \left\{ \text{Tr}\left[\tilde{O}^{(i)}\Gamma_j^{(n)}\tilde{O}^{(i)}\left(\Gamma_j^{(n)}\right)^T\right] \right.$$

$$\left. \mp \text{Tr}\left[\tilde{O}^{(i)}\Gamma_j^{(n)}\tau_3 1_4 \tilde{O}^{(i)}\tau_3 1_4 \left(\Gamma_j^{(n)}\right)^T\right] \right\} \frac{m^*}{4\pi}, \quad \text{(C35)}$$

$$\tilde{B}_{ij}^{(3/4)} = -\frac{1}{32} \sum_{n=1}^{m_j} \left\{ \text{Tr}\left[\tilde{O}^{(i)}\Gamma_j^{(n)} 1\sigma_1 1 \tilde{O}^{(i)} 1\sigma_1 1 \left(\Gamma_j^{(n)}\right)^T\right] \right.$$

$$\pm \text{Tr}\left[\tilde{O}^{(i)}\Gamma_j^{(n)}\tau_3\sigma_1 1 \tilde{O}^{(i)}\tau_3\sigma_1 1 \left(\Gamma_j^{(n)}\right)^T\right]$$

$$\mp \text{Tr}\left[\tilde{O}^{(i)}\Gamma_j^{(n)} 1\sigma_2 1 \tilde{O}^{(i)} 1\sigma_2 1 \left(\Gamma_j^{(n)}\right)^T\right]$$

$$\left. - \text{Tr}\left[\tilde{O}^{(i)}\Gamma_j^{(n)}\tau_3\sigma_2 1 \tilde{O}^{(i)}\tau_3\sigma_2 1 \left(\Gamma_j^{(n)}\right)^T\right] \right\} \frac{m^*}{4\pi}. \quad \text{(C36)}$$

Now we consider corrections to the *finite* applied electric field; see Eq. (79). In this case, we find that the lowest-order corrections come from the *first-order* term in the cumulant expansion; these first-order corrections would be zero in the absence of the electric field. They are represented by "tadpole" and "sunrise" diagrams, as shown in Fig. 13. The contribution from the "tadpole" diagrams is

$$\delta S_t = -\sum_S g_S \int_{\mathbf{k}'_<,\omega'} \int_{\mathbf{k}_>,\omega} \text{Tr}[S1 G_{\mathbf{k}}(i\omega)] \psi_{\mathbf{k}'}^\dagger(\omega') S 1 \psi_{\mathbf{k}'}(\omega').$$

(C37)

The integral over $\mathbf{k}$ and sum over ω can be evaluated using Eq. (B16). The trace occurring in this expression is only nonzero if $S = 1\sigma_3$. Therefore we only generate a correction to the applied electric field. Since $1\sigma_3 1 = \Gamma_5^{(1)}$, we see that the

only nonzero contribution from this term to the coefficients b_i in Eq. (79) is to b_5, and this contribution is $b_5(\text{tadpole}) = 8 \times \frac{m^*}{4\pi}$.

The "sunrise" diagrams give us

$$\delta S_s = \sum_S g_S \int_{\mathbf{k}'_<,\omega'} \int_{\mathbf{k}_>,\omega} \psi_{\mathbf{k}'}^\dagger(\omega') S 1 G_{\mathbf{k}}(i\omega) S 1 \psi_{\mathbf{k}'}(\omega').$$

(C38)

The matrix occurring in this expression is proportional to $1\sigma_3 1$, and thus we, once again, only generate corrections to the applied electric field. This will contribute to all of the b_i. These contributions are given by

$$b_i(\text{sunrise}) = \frac{1}{8} \sum_m \text{Tr}\left(1\sigma_3 1\Gamma_i^{(m)} 1\sigma_3 1\Gamma_i^{(m)}\right) \frac{m^*}{4\pi}. \quad \text{(C39)}$$

The total value of b_i is simply the sum of the above two contributions, i.e., $b_i = b_i(\text{tadpole}) + b_i(\text{sunrise})$.

APPENDIX D: COEFFICIENTS IN THE FREE ENERGY

The coefficients $\alpha_{a,i}^{\text{ph}}$ appearing in the free energy, Eq. (35), are

$$\alpha_{1/2,i}^{\text{ph}} = 8 \pm \text{Tr}[(O^{(i)}\tau_3 1_4)^2], \quad \text{(D1)}$$

$$\alpha_{3/4,i}^{\text{ph}} = -\frac{1}{2} \{ \text{Tr}[(O^{(i)} 1\sigma_1 1)^2] \mp \text{Tr}[(O^{(i)}\tau_3\sigma_1 1)^2]$$

$$\mp \text{Tr}[(O^{(i)} 1\sigma_2 1)^2] + \text{Tr}[(O^{(i)}\tau_3\sigma_2 1)^2] \}. \quad \text{(D2)}$$
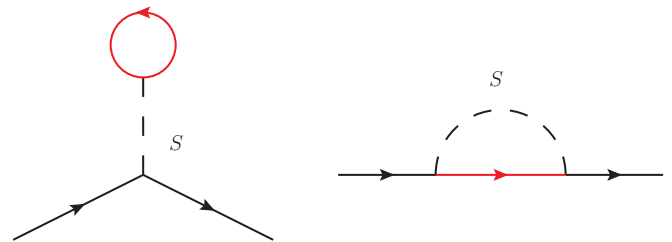

FIG. 13. (Color online) Diagrams representing contributions to the renormalization of the applied electric field term. All lines are as in Fig. 12.

The $\alpha_{a,i}^{\rm pp}$ coefficients are

$$\alpha_{1/2,i}^{\rm pp} = 8 \mp {\rm Tr}[(\tilde{O}^{(i)}\tau_3 1_4)^2], \tag{D3}$$

$$\alpha_{3/4,i}^{\rm pp} = \frac{1}{2}\{{\rm Tr}[(\tilde{O}^{(i)}1\sigma_1 1)^2] \pm {\rm Tr}[(\tilde{O}^{(i)}\tau_3\sigma_1 1)^2]$$
$$\mp {\rm Tr}[(\tilde{O}^{(i)}1\sigma_2 1)^2] - {\rm Tr}[(\tilde{O}^{(i)}\tau_3\sigma_2 1)^2]\}. \tag{D4}$$

APPENDIX E: ANALYTIC DETERMINATION OF THE PHASE BOUNDARIES IN THE FIXED RATIO PLANE

We will now describe how we determined the phase boundaries in the target plane. These boundaries are defined by the sign of the susceptibility exponent γ_i, as given by Eq. (48),

for a given phase; whenever it is positive, we say that the associated phase is present. The value of $\mathcal{A}_{(E_g)}$ is given by Eq. (71). We may obtain $\mathcal{B}_{i,(E_g)}$ from Eqs. (33) and (34) and from the coupling constant ratios $\rho_i^{(E_g)}$ given in Eqs. (68)–(70). Because of this, all of the γ_i will have the form

$$\gamma_i = \frac{Q_i(x,y)}{3 + 2x + 3x^2 + 4y + 4xy + 8y^2}, \tag{E1}$$

where $Q_i(x,y)$ is an inhomogeneous quadratic function of x and y. The denominator of this expression is positive definite, so that the sign of the exponent is determined entirely by $Q_i(x,y)$. Our condition that γ_i be positive thus requires that $Q_i(x,y) > 0$. We therefore see that the phase boundaries, given by $Q_i(x,y) = 0$, are all conic sections.

[1] T. Giamarchi, *Quantum Physics in One Dimension* (Oxford University Press, New York, NY, 2004).

[2] E. McCann and V. I. Fal'ko, Phys. Rev. Lett. **96**, 086805 (2006).

[3] A. H. Castro Neto, F. Guinea, N. M. R. Peres, K. S. Novoselov, and A. K. Geim, Rev. Mod. Phys. **81**, 109 (2009).

[4] R. T. Weitz, M. T. Allen, B. E. Feldman, J. Martin, and A. Yacoby, Science **330**, 812 (2010).

[5] J. Martin, B. E. Feldman, R. T. Weitz, M. T. Allen, and A. Yacoby, Phys. Rev. Lett. **105**, 256806 (2010).

[6] A. S. Mayorov, D. C. Elias, M. Mucha-Kruczyński, R. V. Gorbachev, T. Tudorovskiy, A. Zhukov, S. V. Morozov, M. I. Katsnelson, V. I. Fal'ko, A. K. Geim, and K. S. Novoselov, Science **333**, 860 (2011).

[7] J. Velasco, Jr., L. Jing, W. Bao, Y. Lee, P. Kratz, V. Aji, M. Bockrath, C. N. Lau, C. Varma, R. Stillwell, D. Smirnov, F. Zhang, J. Jung, and A. H. MacDonald, Nat. Nanotechnology **7**, 156 (2012).

[8] F. Freitag, J. Trbovic, M. Weiss, and C. Schönenberger, Phys. Rev. Lett. **108**, 076602 (2012).

[9] A. Veligura, H. J. van Elferen, N. Tombros, J. C. Maan, U. Zeitler, and B. J. van Wees, Phys. Rev. B **85**, 155412 (2012).

[10] W. Bao, J. Velasco, Jr., F. Zhang, L. Jing, B. Standley, D. Smirnov, M. Bockrath, A. MacDonald, and C. N. Lau, Proc. Natl. Acad. Sci. USA **109**, 10802 (2012).

[11] O. Vafek and K. Yang, Phys. Rev. B **81**, 041401 (2010).

[12] O. Vafek, Phys. Rev. B **82**, 205106 (2010).

[13] R. Shankar, Rev. Mod. Phys. **66**, 129 (1994).

[14] K. G. Wilson, Phys. Rev. B **4**, 3174 (1971).

[15] R. E. Throckmorton and O. Vafek, arXiv:1111.2076v2.

[16] Y. Lemonik, I. L. Aleiner, C. Toke, and V. I. Fal'ko, Phys. Rev. B **82**, 201408 (2010).

[17] Y. Lemonik, I. L. Aleiner, and V. I. Fal'ko, Phys. Rev. B **85**, 245451 (2012).

[18] S. Chakravarty, B. I. Halperin, and D. R. Nelson, Phys. Rev. B **39**, 2344 (1989).

[19] A. J. Millis, Phys. Rev. B **48**, 7183 (1993).

[20] O. Vafek, Bulletin of the APS March Meeting 2012 57, Number 1; http://meetings.aps.org/link/BAPS.2012.MAR.Z27.1.

[21] Yu. A. Bychkov, L. P. Gorkov, and I. E. Dzyaloshinskii, Sov. Phys. JETP **23**, 489 (1966).

[22] I. E. Dzyaloshinskii and A. I. Larkin, Sov. Phys. JETP **34**, 422 (1972).

[23] M. Gaudin, Phys. Lett. A **24**, 55 (1967).

[24] C. N. Yang, Phys. Rev. Lett. **19**, 1312 (1967).

[25] E. H. Lieb and F. Y. Wu, Phys. Rev. Lett. **20**, 1445 (1968).

[26] C. N. Yang, Phys. Rev. Lett. **63**, 2144 (1989).

[27] S. C. Zhang, Phys. Rev. Lett. **65**, 120 (1990).

[28] C. N. Yang and S. C. Zhang, Mod. Phys. Lett. B **4**, 759 (1990).

[29] A. Auerbach, *Interacting Electrons and Quantum Magnetism* (Springer Verlag, New York, NY, 1994).

[30] J. E. Hirsch and S. Tang, Phys. Rev. Lett. **62**, 591 (1989).

[31] A. Moreo, D. J. Scalapino, R. L. Sugar, S. R. White, and N. E. Bickers, Phys. Rev. B **41**, 2313 (1990).

[32] A. Moreo and D. J. Scalapino, Phys. Rev. Lett. **66**, 946 (1991).

[33] C. M. Varma, Phys. Rev. Lett. **61**, 2713 (1988).

[34] H. Min, G. Borghi, M. Polini, and A. H. MacDonald, Phys. Rev. B **77**, 041407(R) (2008).

[35] F. Zhang, H. Min, M. Polini, and A. H. MacDonald, Phys. Rev. B **81**, 041402(R) (2010).

[36] R. Nandkishore and L. Levitov, Phys. Rev. Lett. **104**, 156803 (2010).

[37] R. Nandkishore and L. Levitov, Phys. Rev. B **82**, 115124 (2010).

[38] J. Jung, F. Zhang, and A. H. MacDonald, Phys. Rev. B **83**, 115408 (2011).

[39] E. V. Gorbar, V. P. Gusynin, V. A. Miransky, and I. A. Shovkovy, arXiv:1204.2286v1.

[40] L. M. Zhang, Z. Q. Li, D. N. Basov, M. M. Fogler, Z. Hao, and M. C. Martin, Phys. Rev. B **78**, 235408 (2008).

[41] J. Nilsson, A. H. Castro Neto, F. Guinea, and N. M. R. Peres, Phys. Rev. B **78**, 045405 (2008).

[42] M. Tinkham, *Group Theory and Quantum Mechanics* (Dover, New York, NY, 2003).

[43] F. D. M. Haldane, Phys. Rev. Lett. **61**, 2015 (1988).

[44] L. Zhu, V. Aji, and C. M. Varma, arXiv:1202.0821v1.

[45] C. Y. Hou, C. Chamon, and C. Mudry, Phys. Rev. Lett. **98**, 186809 (2007).

[46] M. M. Scherer, S. Uebelacker, and C. Honerkamp, Phys. Rev. B **85**, 235408 (2012).

[47] M. Kharitonov, arXiv:1109.1553v2.

[48] D. R. Nelson, Phys. Rev. B **11**, 3504 (1975).

[49] F. Y. Wu, Rev. Mod. Phys. **54**, 235 (1982).

[50]Due to the Mermin-Wagner argument, if there is a coexistence of the nematic with AF/QSH, then it can only appear at $T = 0$, since, unlike the nematic, which breaks a discrete symmetry ($D_{3d} \rightarrow C_i$), AF and QSH break a continuous $O(3)$ symmetry. We see no reason why such a putative line could not end at a finite value of $g_{A_{1g}}$ marked by the question mark.

[51]F. Zhang, H. Min, and A. H. MacDonald, arXiv:1205.5532v1.

[52]M. E. Peskin and D. V. Schroeder, *An Introduction to Quantum Field Theory* (Westview, Boulder, CO, 1995), p. 406.

[53]J. Cardy, *Scaling and Renormalization in Statistical Physics* (Cambridge University Press, New York, NY, 1996).

[54]H. J. Schulz, Phys. Rev. Lett. **64**, 2831 (1990).